Cell

Ultrafast distant wound response is essential for whole-body regeneration

Graphical abstract

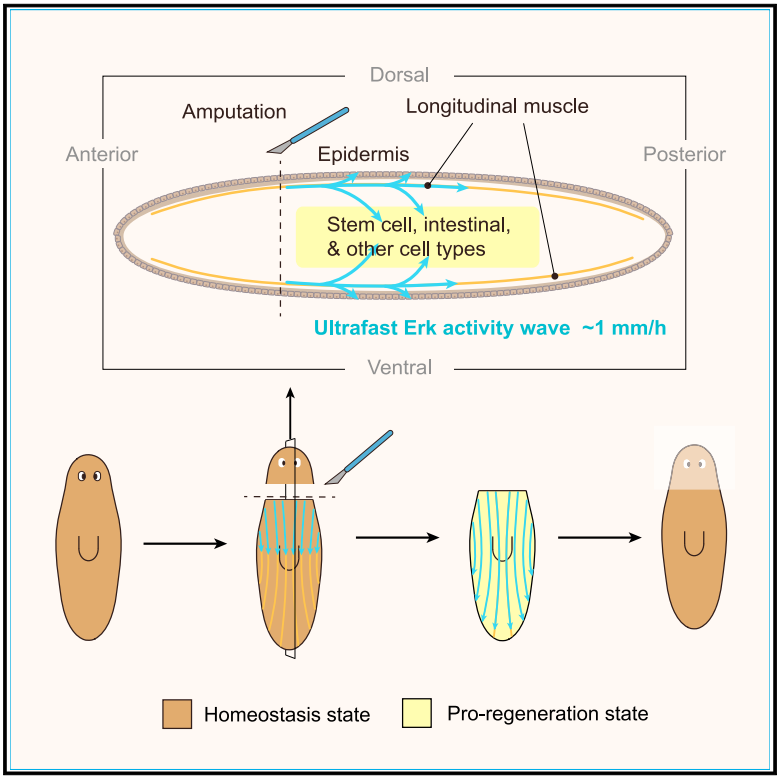

Authors

Yuhang Fan, Chew Chai, Pengyang Li, Xinzhi Zou, James E. Ferrell, Jr., Bo Wang

Correspondence

wangbo@stanford.edu

In brief

Longitudinal body-wall muscles act as superhighways for propagating and disseminating wound signals for systemic responses to enable planarian regeneration.

Highlights

- Wound responses are coordinated over long distances via ultrafast Erk activity wave
- Whole-body regeneration requires feedback between tissues at and far from wounds
- Planarian longitudinal muscles are superhighways for propagating Erk activity
- Muscles relay wound signals to other cell types, instructing responses therein

Fan et al., 2023, Cell *186*, 3606–3618
August 17, 2023
https://doi.org/10.1016/j.cell.2023.06.019

CellPress

CellPress

Cell

Article

Ultrafast distant wound response is essential for whole-body regeneration

Yuhang Fan,[1] Chew Chai,[1] Pengyang Li,[1] Xinzhi Zou,[1] James E. Ferrell, Jr.,[2,3] and Bo Wang[1,4,*]
[1]Department of Bioengineering, Stanford University, Stanford, CA, USA
[2]Department of Chemical and Systems Biology, Stanford University School of Medicine, Stanford, CA, USA
[3]Department of Biochemistry, Stanford University School of Medicine, Stanford, CA, USA
[4]Lead contact
*Correspondence: wangbo@stanford.edu
https://doi.org/10.1016/j.cell.2023.06.019

SUMMARY

Injury induces systemic responses, but their functions remain elusive. Mechanisms that can rapidly synchronize wound responses through long distances are also mostly unknown. Using planarian flatworms capable of whole-body regeneration, we report that injury induces extracellular signal-regulated kinase (Erk) activity waves to travel at a speed 10–100 times faster than those in other multicellular tissues. This ultrafast propagation requires longitudinal body-wall muscles, elongated cells forming dense parallel tracks running the length of the organism. The morphological properties of muscles allow them to act as superhighways for propagating and disseminating wound signals. Inhibiting Erk propagation prevents tissues distant to the wound from responding and blocks regeneration, which can be rescued by a second injury to distal tissues shortly after the first injury. Our findings provide a mechanism for long-range signal propagation in large, complex tissues to coordinate responses across cell types and highlight the function of feedback between spatially separated tissues during whole-body regeneration.

INTRODUCTION

It has long been noted that injury can induce responses in uninjured tissues far from wounds.[1–4] In many invertebrates, injury triggers proliferation in cells both nearby and millimeters to centimeters away,[5,6] suggesting that wound signals can spread across long distances even though these organisms lack a circulatory system. In mouse, injury to muscles in one leg causes stem cells in the contralateral leg to switch from quiescence to an alert state, which may prepare tissues for future injuries.[7,8] Similar effects have been observed after axolotl limb amputation, implicating that long-range induction of wound responses may be a broadly conserved phenomenon.[9,10] More recently, cardiac injury in zebrafish was shown to induce coordinated gene expression changes in distant organs including the brain and kidney controlled by a single permissive enhancer, but attempts to eliminate the distal (DS) responses did not alter the heart regeneration outcome.[11] Thus, although systemic wound responses appear to be widespread, it remains unclear whether they contribute to the current round of regeneration or simply represent byproducts of injury-induced signaling cascades.

In order to participate in regeneration, DS wound responses need to turn on shortly after injury within the right time window as the regeneration proceeds. This timescale should be determined by the rate at which wound signals are communicated between injury and distant sites. However, besides circulatory factors,[8,12,13] mechanisms that can rapidly transmit molecular signals over millimeter-to-centimeter distances in nonvascularized tissues are largely unknown.

Although wound signals may spread in the form of diffusive cues,[14–16] a long-standing puzzle is that diffusion is often too short-ranged in densely packed tissues.[17] It has been recently shown that coupling diffusion with biochemical positive feedbacks can induce trigger waves and help to overcome some limitations of simple diffusion.[18–20] However, due to slow intercellular communication in multicellular tissues, the observed propagation speeds of these waves, ~10–100 μm/h,[18,19] are still incompatible with the fast, long-range communication required by regeneration programs that need to rapidly progress in time.

To study the coordination and function of systemic wound responses, we investigate the planarian flatworm *Schmidtea mediterranea*, which has a remarkable ability to regenerate essentially any missing body parts.[21–23] They can regrow into normal healthy organisms from minute tissue remnants on a timescale of days. Injury induces broad transcriptional changes throughout the animal.[24] Accompanying these global molecular responses is elevated stem cell proliferation,[6] followed by the re-establishment of body polarity via position-control genes[25] and the induction of transient regeneration-activated cell states in various tissues.[26] These wound responses and their downstream processes are essential to drive the differentiation of new tissues and initiate the remodeling of existing tissues.

We sought to understand how this long-range coordination arises and whether the wound responses in uninjured tissues are required for regeneration. We found the wound signal to propagate in the form of an extracellular signal-regulated kinase (Erk) wave that travels at an unexpected speed (~1 mm/h) 10–100 times faster than those reported in other multicellular tissues.[18,19] The ultrafast propagation of Erk activity requires the longitudinal body-wall muscles, which act as superhighways for signal transduction and relay the wound signal to other cell types instructing responses therein. Combining experiments and a theoretical model, we proposed that the morphological properties of muscle cells, i.e., close packing of parallel elongated cell bodies, provide the cellular basis needed for rapid long-range communication. Inhibiting Erk activity propagation and thereby DS wound responses blocked the planarian regeneration, which can be rescued by inducing wound responses through a second amputation of DS tissues within a narrow time window after the first injury. These findings suggest that proximal (PR) responses alone are insufficient to drive regeneration, and timely long-range feedback between spatially separated tissues is essential for whole-body regeneration.

RESULTS

Rapid spatial coordination of wound responses is mediated by ultrafast Erk activity wave

To better characterize the spatial coordination of planarian wound responses at the systems level, we performed RNA sequencing (RNA-seq) on tails after amputating tail and head regions respectively (Figure 1A). This experiment allowed us to quantitatively compare responses PR and DS to wounds within the same tissue. Although the PR responses were more pronounced initially, we observed a strong correlation between the PR and DS responses at 6 h post amputation (hpa) (Figures 1B, 1C, and S1A), except for a focal set of genes specifically induced at wounds (Figure 1C). Such global correlation was maintained at 24 hpa even though the upregulated genes were different, highlighting the highly dynamic transcriptional changes during regeneration (Figures S1B and S1C). These results suggest that although wound signal takes time to reach DS tissues, upon arrival, it elicits responses that largely resemble those at the injury site.

Planarian wound responses depend upon the activation of Erk (Figures S1D and S1E),[27,28] via a highly conserved wound repair pathway.[29–32] This raises the possibility that Erk signaling is responsible for coordinating planarian wound responses in space and time. Indeed, in mouse skin[18] and zebrafish scales,[19] Erk activity can be relayed between cells in the form of trigger waves after injury (Figure S1F). Trigger waves are self-regenerating fronts of activity produced in signaling systems with positive feedback, and they spread without losing speed or amplitude, making them suitable for long-range signaling.[33–36] However, the reported wave speeds (~10–100 μm/h) are orders of magnitude too slow to explain the rapid activation of DS wound responses in the planarian. It would take days or even weeks for the signal to travel across the planarian body, which is typically 5–20 mm long.

In addition, previous studies of Erk waves in multicellular systems have focused on tissues comprising uniform cell populations.[18–20,37,38] By contrast, planarian wound responses need to be coordinated across various cell types that may have different sensing mechanisms, activation kinetics, and competency in transmitting the signal. Indeed, using single-cell RNA-seq (scRNA-seq) on tissues at 3 hpa in the presence or absence of the Erk kinase (Mek) inhibitor U0126 (Figure S2), we found that, along with cell type-specific responses (e.g., activation of *mcm7* in neoblasts, *mkpA* in muscles and neurons), generic wound responses (e.g., activation of *tnf-1*, *jun 1*) were induced in most cell types after injury (Figures 1D, 1E, and S3). These responses were abolished after inhibiting Erk, suggesting that their induction is Erk dependent.

These reservations notwithstanding, we examined whether Erk signal propagates in a wave-like manner in planarian tissues after injury. We quantified Erk activity (defined by the ratio between phosphorylated Erk, pErk, and total Erk) in tissue pieces evenly spaced ~1 mm apart using western blotting (Figures 2A, S4A, and S4B). In line with the timing of the transcriptional changes (Figures 1B and 1C), Erk activity peaked around 0.5 hpa in tissues PR to wounds and propagated distally with ~1 h delay in peak time between adjacent positions (Figures 2A, 2B, and S4C). The linear relationship between peak time and distance from wounds is consistent with wave propagation. In addition, the signal did not dampen with distance traveled (Figures 2A, 2B, and S4D). This can account for the high correlation between PR and DS transcriptional wound responses (Figure 1B).

From the time and distance relationship, we measured the wave speed to be ~1 mm/h (Figure 2C), which is 1–2 orders of magnitude faster than reported values in other multicellular tissues[18–20] but comparable to the speed of some intracellular trigger waves in large cells.[39,40] This speed was independent of propagation direction—that is, Erk activity could spread either from head to tail or from tail to head, depending on where the wound was located (Figures 2D, S4E, and S4F)—and was independent of animal size (Figures 2E, S4G, and S4H). These findings suggest that wave speed is controlled by the intrinsic properties of a bidirectional signaling system.

DS wound responses are essential for regeneration

One prediction of trigger wave models is that the speed of Erk wave should be reduced by partially inhibiting the intracellular Erk cascade.[35,37] Consistent with this prediction, Erk activation in DS tissues was significantly delayed with increasing Mek inhibitor (U0126) concentrations and was eventually blocked when the U0126 concentration exceeded a critical threshold (~8 μM), whereas Erk activity was only slightly reduced at wounds through a broad range of inhibitor concentrations (Figures 3A and 3B). This allowed us to evaluate regeneration phenotypes while tuning the rate of Erk activity propagation and to separate the contributions of PR and DS wound responses during regeneration.

We found that blocking Erk propagation inhibited stem cell mitosis only in DS tissues post amputation, but left proliferation at wounds unaffected (Figures 3C and S4I). This result establishes a direct link between Erk activation and stem cell

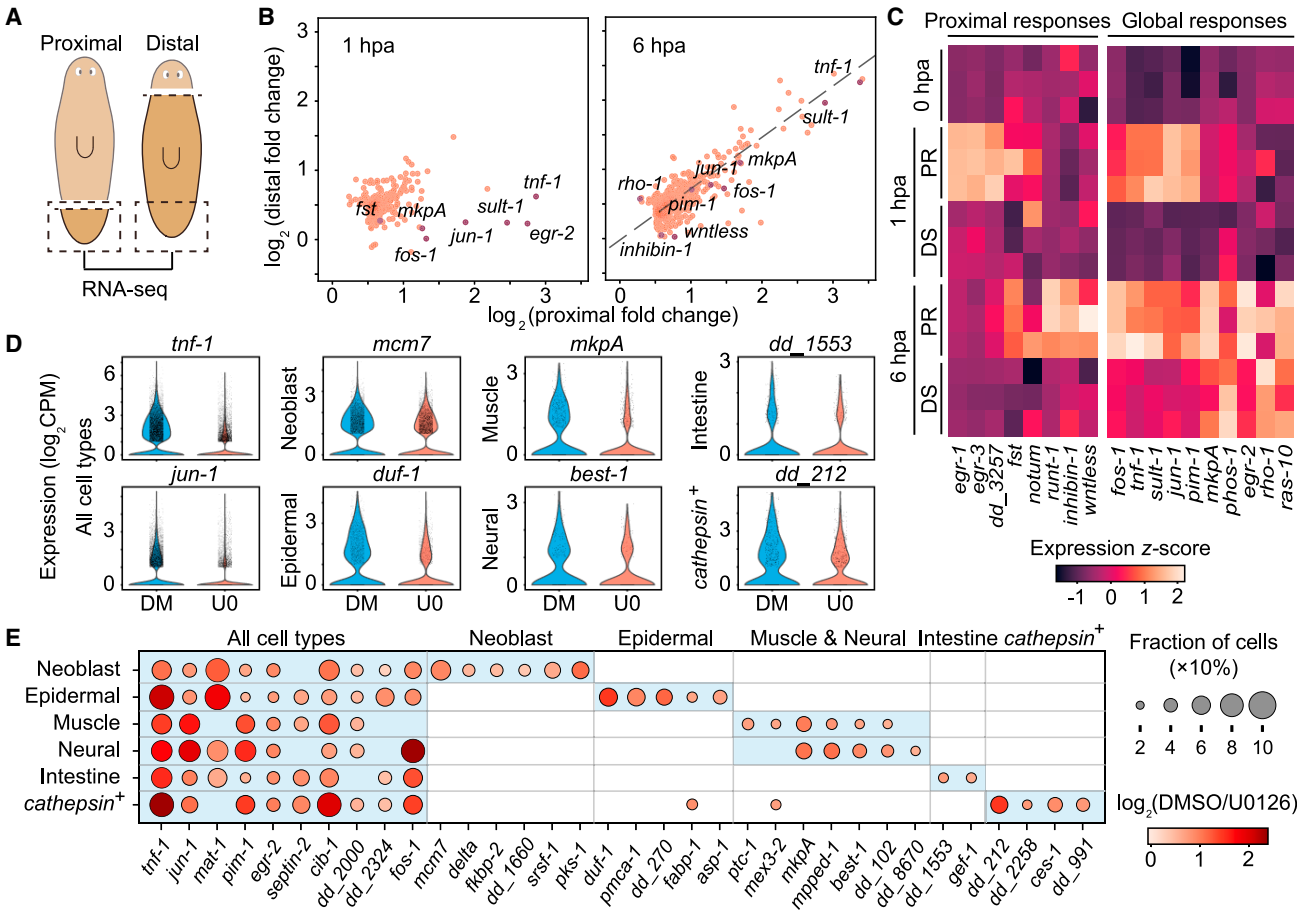

Figure 1. Coordination of planarian wound responses across long distances and cell types

(A) Strategy to measure proximal and distal wound responses in the same tissue.

(B) Comparison of gene upregulation proximal and distal to wounds. Genes plotted have p value < 0.001 (two-sided Welch's t test) and $\log_2$(fold change) > 0.5 in either proximal or distal samples, measured from three biological replicates each containing five ~5 mm long animals.

(C) Heatmap showing example upregulated genes. Proximal responses (PR) include genes activated in proximal tissues (p value < 0.01, two-sided Welch's t test, three biological replicates each containing five ~5 mm long animals) but not activated in distal tissues (DS, p value > 0.05, two-sided Welch's t test). Global responses include genes activated in both proximal and distal responses.

(D) Violin plots showing expression distribution of representative wound response genes, measured in animals treated by DMSO (DM, blue) or 25 μM U0126 (U0, orange) to completely block Erk activation. Points: data of individual cells. Genes shown are downregulated in U0126 treated samples (p value < 0.01, two-sided Mann-Whitney-Wilcoxon test) in cell types specified.

(E) Expression fold changes of Erk-dependent wound response genes in individual cell types. Genes shown are downregulated by U0126 treatment (p value < 0.01, two-sided Mann-Whitney-Wilcoxon test) in specific cell types according to the scRNA-seq data. These genes are also upregulated at 6 hpa globally measured by bulk RNA-seq (p value < 0.001, two-sided Welch's t test, Figure S1D). In (D) and (E), control and U0126-treated groups contain cells dissociated from thirty animals each, which were pooled to sequence in one batch.

See also Figures S1, S2, and S3 and Tables S2 and S3.

proliferation. The expression of position-control genes, including *notum*, *secreted frizzled related protein 1* (*sFRP-1*), and *nou-darake/FGF receptor-like 3* (*ndl-3*),[23] which reestablishes the body plan during regeneration, was strongly perturbed in the absence of Erk propagation (Figures 3D and S4J–S4L). Accordingly, regeneration of anterior tissues such as *opsin*$^+$ photoreceptors after decapitation was delayed with slower Erk propagation and absent when Erk activation was blocked in DS tissues, though the epidermis (*NB.22.1E*$^+$) eventually closed over wounds at a much later time (Figure 3D). To quantify the rate of regeneration, we counted *cintillo*$^+$ chemosensory neurons regenerated at 7 days post amputation (dpa) and found that their numbers decreased with reduced Erk propagation until dropping to zero in animals treated with U0126 above the critical concentration (Figure 3E).

We noticed that Erk activity propagation was most critical to regeneration when wound responses needed to be activated across long distances. When we sliced planarians such that the majority of the remaining tissues had been exposed to injury, regeneration was less sensitive to U0126 treatment, as the PR wound responses were mostly unaffected around the critical inhibitor concentration (Figure 4A).

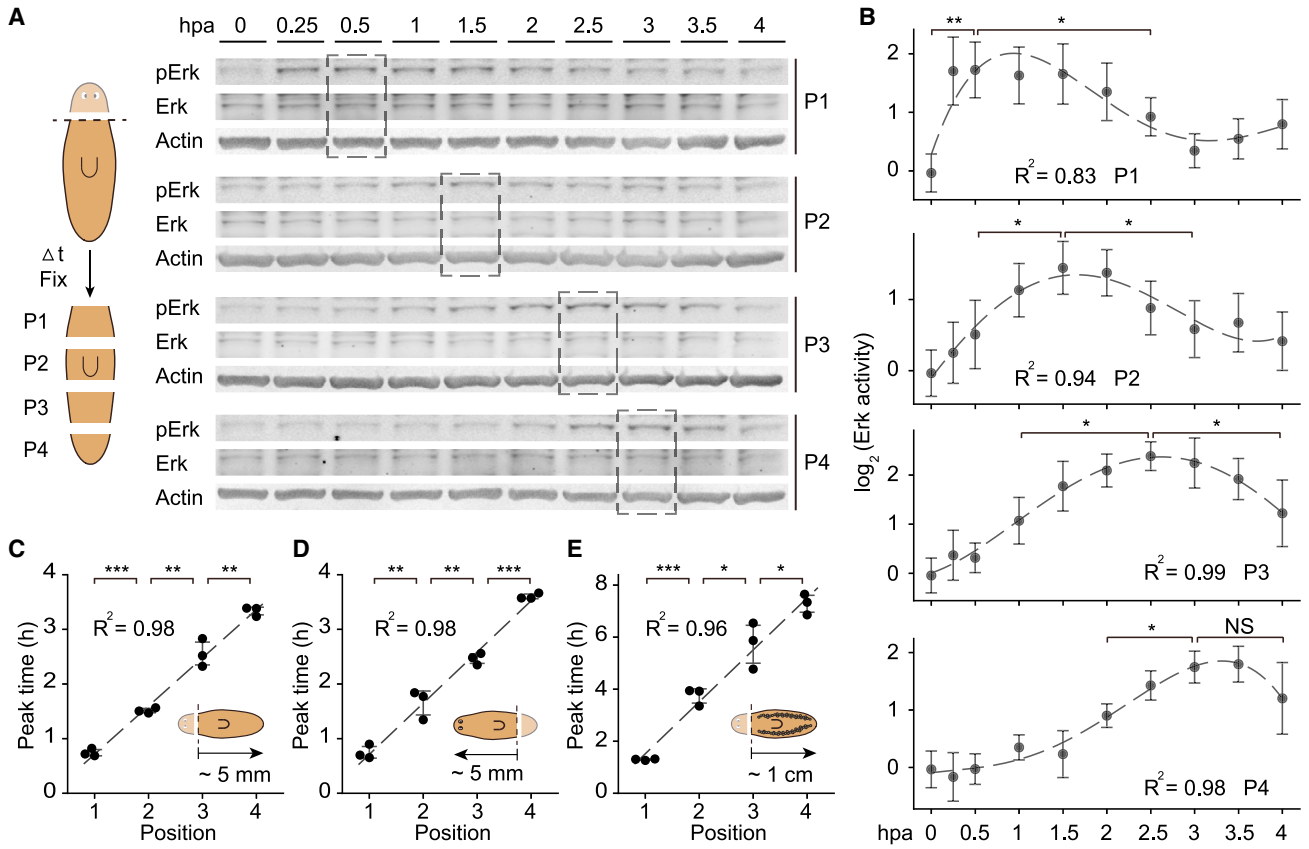

Figure 2. Ultrafast propagation of Erk activity after injury

(A) (Left) Schematic showing the strategy to measure spatiotemporal propagation of Erk activity in planarian tissues. At specified time points after amputation, animals were fixed and cut into four pieces (P1–4 from proximal to distal) along anterior-posterior (A-P) axis. (Right) Representative western blot images of pErk, total Erk, and actin (loading control) on tissues at different positions (P1–4) throughout the first 4 hpa from three replicates of ten tissue fragments at each A-P position. Dashed boxes: maximum Erk activity at each position.

(B) Quantification of Erk activity from western blotting, using the ratio between pErk and total Erk intensities. Dashed lines: least squares polynomial fit. R^2: coefficients of determination. *$p < 0.05$; **$p < 0.01$; NS, no significant difference; one-sided Welch's t test using the hypothesis that the peak activity is higher than those at compared time points.

(C–E) Erk activity peak times vs. proximal-to-distal position. Insets: planarians of the asexual biotype of ~5 mm in length are amputated anteriorly (C) and posteriorly (D), and the animals of the sexual biotype of ~1 cm in length are amputated posteriorly (E). Each data point represents a biological replicate using tissue fragments from ten animals. Dashed line: linear fit. *$p < 0.05$; **$p < 0.01$; ***$p < 0.001$, two-sided Welch's t test. Error bars: standard derivation (SD).
See also Figure S4.

Motivated by this surprising result and given that DS and PR wound responses are largely correlated, we reasoned that inducing responses in DS tissues through the second injury may compensate for the lack of long-range coordination of wound responses. Whereas the delay time between PR and DS responses under natural conditions should be defined by the speed of wound signals propagation, using two amputations separated in time (Figure 4B), we can tune the delay between the first and second injury to investigate the effects of temporal coordination of wound responses.

To test this hypothesis, we decapitated the planarians treated with U0126 at 8 μM, which eliminated the DS wound responses, waited for various amounts of time, and then amputated in tail. Strikingly, the second amputation within a few hours after the first amputation was sufficient to rescue the regeneration in a large fraction of animals, whereas the planarians amputated a day after failed to regenerate either head or tail (Figures 4B and 4C). The regeneration was stalled at an early stage before the reset of body polarity, manifested by the lack of *notum* expression and blastema formation. Surprisingly, not only did the first amputation in the heads require the second injury in the tails to regenerate, but tail regeneration from the second amputation also relied on the first injury, which must have occurred not too long before. Altogether, our findings demonstrate that wound responses in tissues distant to wounds rely on the propagation of Erk activity—delayed or missing DS Erk activation can cause regeneration deficiencies, implying that DS tissues may provide feedback to cells at wounds to license regeneration. This feedback needs to occur early on during regeneration, stressing the necessity of ultrafast propagation of Erk activity.

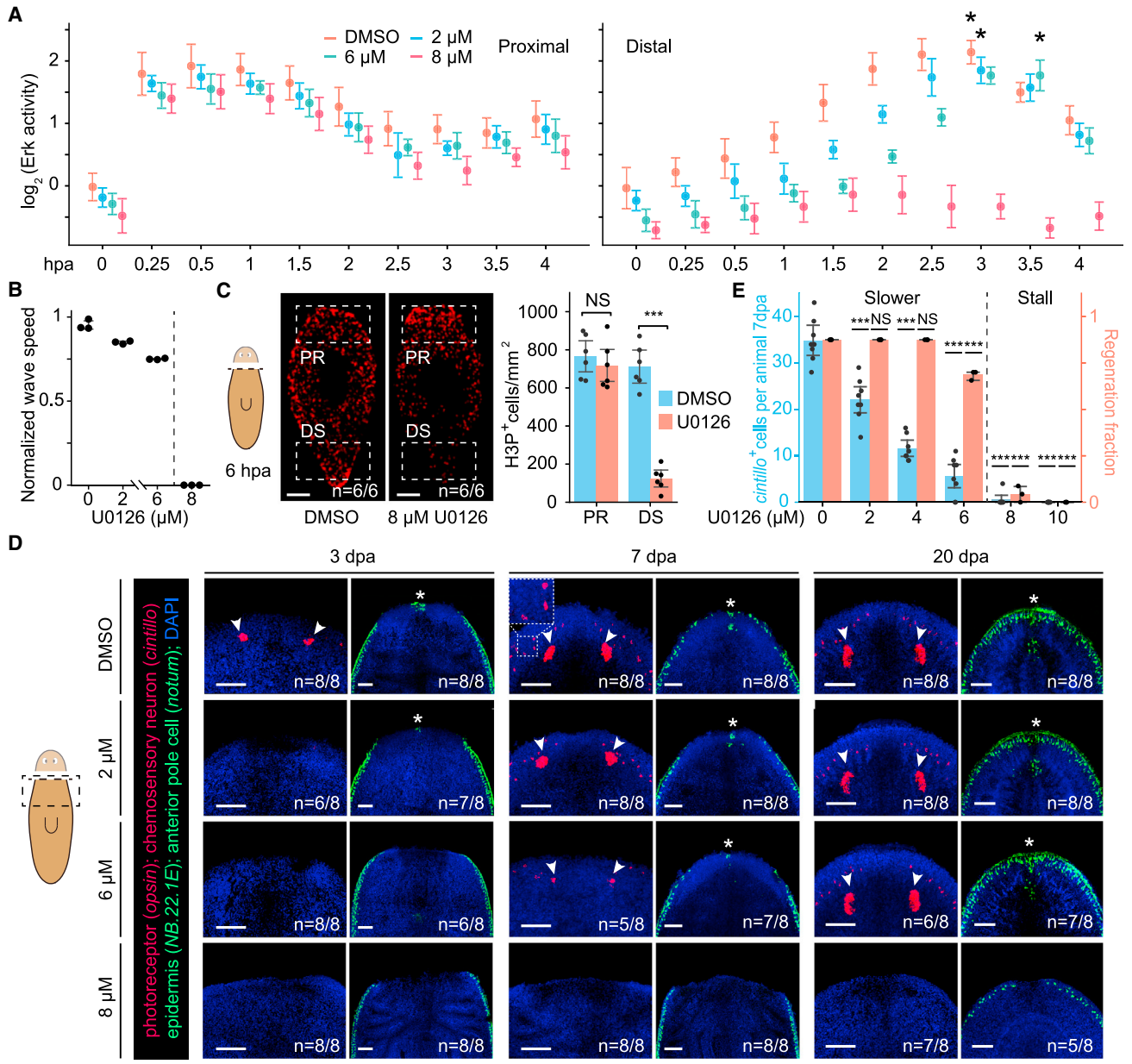

Figure 3. Erk activity propagation is essential to planarian regeneration

(A) Dependence of Erk activity, in tissues proximal (P1, left) and distal (P3, right) to wounds, on U0126 concentration. Asterisks: peak activities in distal responses. Each data point represents three biological replicates containing tissue fragments collected from ten animals.

(B) Fitted Erk activity wave speed vs. U0126 concentration. Each data point represents a biological replicate using ten animals to measure peak time vs. distance from wounds.

(C) (Left) Anti-H3P (phospho-histone H3) labels mitotic cells at 6 hpa in animals treated with DMSO or 8 μM U0126. (Right) Number of $H3P^+$ cells per area in proximal (PR) and distal (DS) regions (boxes in images).

(D) FISH using two sets of pooled probes, red targeting *opsin* (photoreceptor, arrows) and *cintillo* (chemosensory neuron, insets), green targeting *NB.22.1E* (epidermis), and *notum* (anterior pole, asterisks), showing that regeneration of anterior tissues is delayed by increasing concentrations of U0126 and eventually blocked when the U0126 concentration exceeds 8 μM.

(E) Quantification of regeneration progress using the number of regenerated *cintillo*$^+$ neurons at 7 dpa (eight animals per condition, pooled from two independent experiments) and fraction of regenerated animals (three replicates each containing twenty animals) vs. U0126 concentration. In schematics, dashed lines: amputation planes; box: imaging area.

In (C) and (E), ***$p < 0.001$; NS, no significant difference, two-sided Welch's t test; error bars: standard derivation (SD) in (A) and (B), 95% confidence interval (CI) in (C) and (E); n: number of samples consistent with the image out of the total number of samples analyzed, pooled from two independent experiments. Scale bars: 500 μm in (C) and 100 μm in (D).

See also Figure S4 and Table S2.

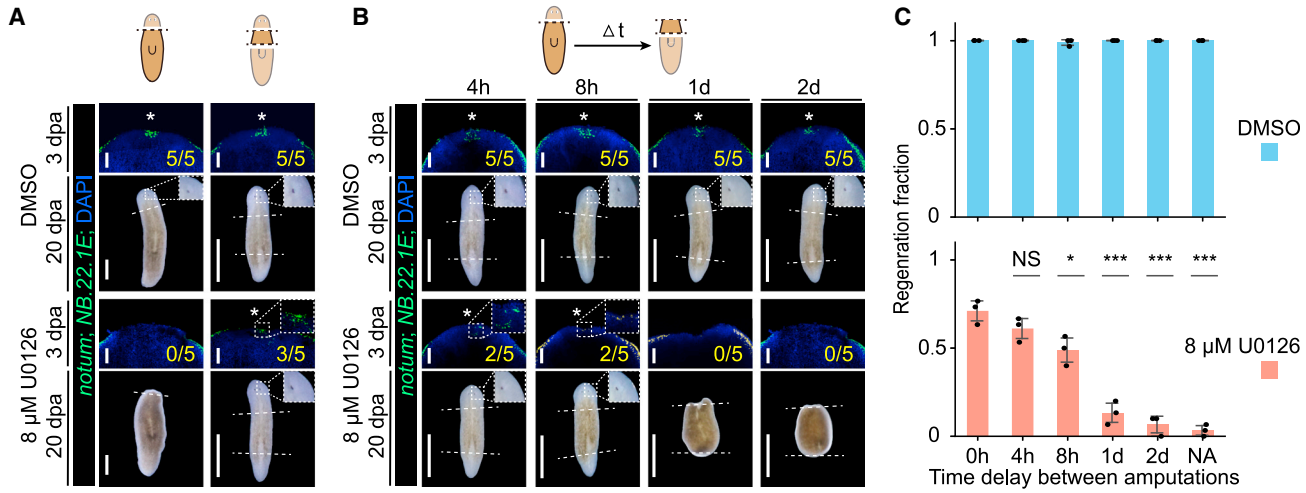

Figure 4. Distal wound responses are essential for planarian regeneration

(A) FISH using pooled probes targeting *notum* (asterisks) and *NB.22.1E* and bright-field images on animals after single amputation (left) or double amputation (right) at 3 and 20 dpa. Animals are treated with either DMSO (top) or 8 μM U0126 (bottom). Anterior regeneration is fully blocked by 8 μM U0126 treatment after single amputation but partially rescued after double amputation. Dashed lines: amputation planes.

(B) FISH images showing *notum* and *NB.22.1E* expression at 3 days after the first amputation and bright-field images of animals at 20 days after the first amputation with second amputation applied at different time points after first amputation. Animals are treated with DMSO (top) or 8 μM U0126 (bottom). Numbers in yellow represent the number of animals with anterior pole regenerated at 3 dpa out of all animal analyzed, pooled from two independent experiments. Scale bars in (A) and (B): 100 μm in fluorescence images and 1 mm in bright-field images.

(C) Fraction of regenerated animals from three replicates each containing thirty animals treated by DMSO (top, blue) or 8 μM U0126 (bottom, orange) vs. time delays between the first and second amputations. NA: no second amputation. *p < 0.05; ***p < 0.001; NS, no significant difference, two-sided Welch's t test comparing against the fraction of regenerated animals in the 0 h delay group; error bars: standard derivation (SD).

Longitudinal body-wall muscles are required for Erk activity propagation and activation of DS wound responses

The observations above raise the question of how Erk activation can propagate so quickly. Studies over decades have shown that in animal cells with typical dimensions—a few pL in volume, with sizes of ~10 μm—stimulation of receptor tyrosine kinases (RTKs) or other upstream Erk regulators results in Erk activation within ~5–10 min in various systems.[41,42] This activation induces the release of activators into the extracellular space to propagate signals between cells (Figure S1F).[43,44] The effective extracellular diffusion coefficient of Erk activator can be estimated on the order of 0.1 $\mu m^2/s$ (see STAR Methods).[18,19,37] This slow diffusion aligns with the fact that Erk activators can bind to the abundant extracellular co-receptors like proteoglycan chains[45,46] but limits the speed of Erk activity wave to be at least one order of magnitude slower than what we observed here. By contrast, multiple mechanisms have been reported to rapidly spread the activation signal intracellularly (see STAR Methods).[47–49] Therefore, we hypothesized that long cell bodies can act as superhighways by minimizing the intercellular components during the relay of Erk signal and might significantly speed up wave propagation (see Figure S5A and STAR Methods for our working model).

This hypothesis can be further formalized using a wave model with cells packed in a one-dimensional space (Figure S5B; STAR Methods), inspired by the classic analysis of the Fisher wave.[50] The key assumption here is that a cell is activated once the activator concentration in a local region of the cell body near its upstream neighbor exceeds a threshold. The rapid intracellular signal propagation then allows the cell to release activator on the other end of its cell body and relay the signal to its downstream neighbor (Figure S5B). This is plausible as previous studies showed that a 0.8 μm sized bead with immobilized epidermal growth factor (EGF) was sufficient to stimulate a cell with EGF receptors on all parts of the cell rapidly activated within 10 s.[47] Our analytical analysis estimated the wave speed to scale with $(L/d)\sqrt{aD}$, which should increase linearly with the cell body length L, normalized by the size of signal sensing region d, and depend on the mean field effective activator release rate, a, and the extracellular diffusion coefficient, D, of the activator. This analysis suggested that cell types with long cell bodies could provide preferred routes for signal propagation in heterogeneous tissues containing cells of a broad range of sizes.

Although most planarian cells are small (~5–10 μm in diameter), the body-wall muscles are mononucleate cells over 100 μm long and assemble into a dense, continuous network covering the whole animal body, with sub-micron spacing between muscle fibers[25,51,52] (Figure 5A). Given that the Erk wave speed is measured to be ~ 1 mm/h in planarian, if propagating cells are of ~100 μm in length, the total time to travel across a long cell should be less than 6 min, matching roughly what is needed for propagating Erk activation signal intracellularly (Figure S5A; STAR Methods).

Indeed, we found that Erk was phosphorylated in most muscle cells after injury (Figures 5A, S5C, and S5D). Ablation of the longitudinal muscles through RNAi-mediated silencing of *myoD* (Figures S5E and S5F), a muscle-specific transcription factor required for longitudinal muscle specification in the planarian,[25]

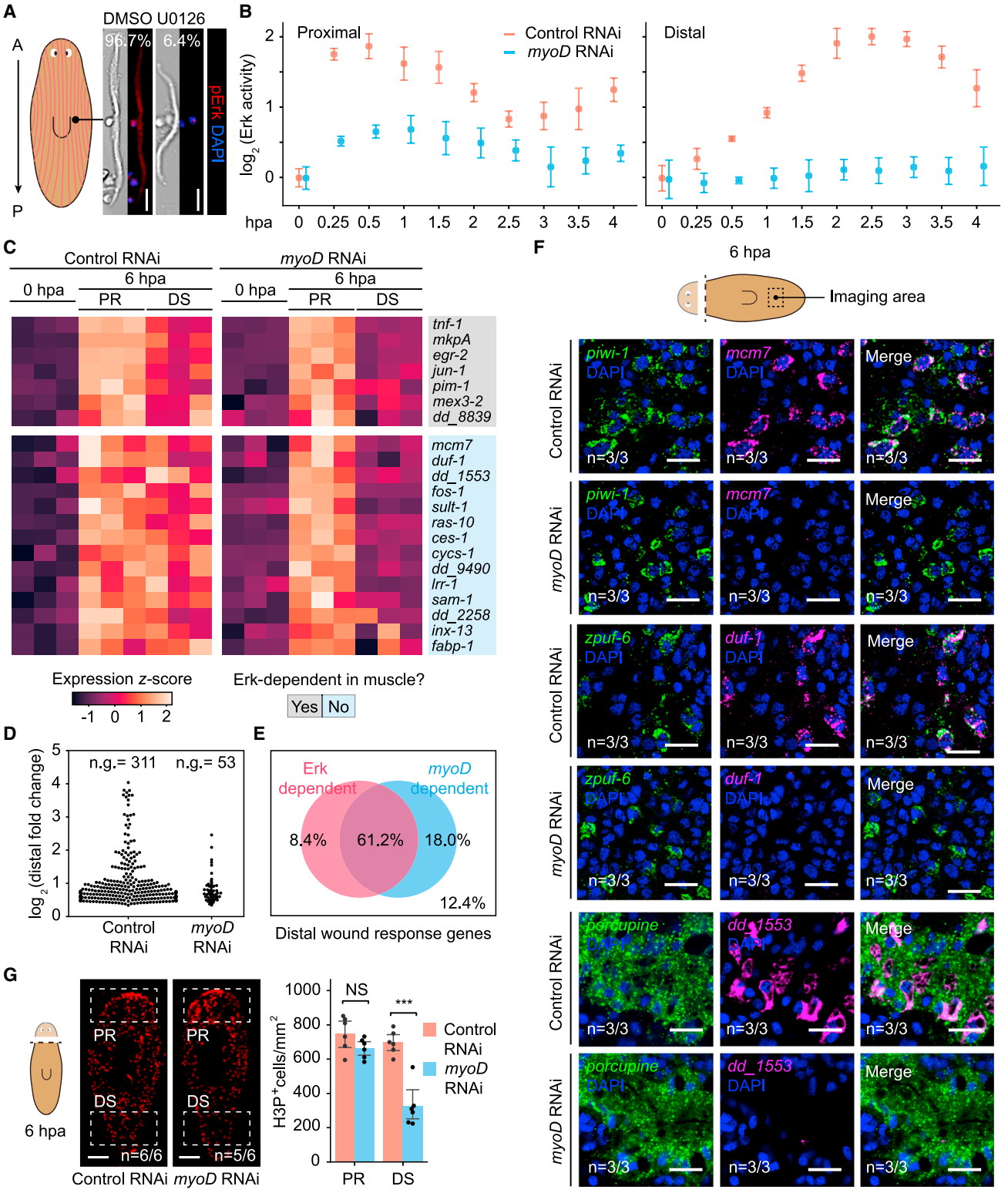

Figure 5. Longitudinal body-wall muscles are required for Erk activity propagation and distal wound responses

(A) (Left) Schematic of planarian longitudinal body-wall muscles (red lines). (Right) Bright-field and pErk immunofluorescence images of muscle cells isolated from wounded planarians (at 3 hpa) treated with DMSO or 25 μM U0126. %, pErk$^+$ fraction of muscle cells.

(legend continued on next page)

led to a marked reduction of Erk activation at wounds, which is consistent with the idea that longitudinal muscles are early responders to injury. *myoD* knockdown also fully blocked injury-induced Erk activation in DS tissues, lending support to our hypothesis (Figures 5B and S5G). Concordantly, >80% of the global wound response genes lost the ability to respond to injury in DS tissues after *myoD* RNAi, though they maintained their responses at PR sites (Figures 5C, 5D, and S5H). As the *myoD*-dependent wound response genes had significant overlap with Erk-dependent genes (Figure 5E), our results suggest that *myoD* RNAi affects wound responses mainly through Erk signaling.

Within the overlap between Erk and *myoD*-dependent wound response genes, many of them were activated only in cell types other than muscles, including *mcm7* in neoblasts, *duf-1* in epidermis, and *dd_1553* in intestine, as revealed by the scRNA-seq analysis (Figures 5C and S1D). Using double fluorescence *in situ* hybridization (FISH), we validated that the activation of these genes in non-muscle cells within DS tissues was blocked after *myoD* RNAi (Figures 5F and S5H). These observations highlight the non-autonomous role of muscle cells, which may function as "pioneers" in transmitting the wound signal and disseminating it to other cell types. At the functional level, stem cell mitotic response in DS tissues was significantly reduced after *myoD* knockdown, whereas proliferation at the wound site was unchanged (Figure 5G), indicating that stem cell activation requires instructions from the muscle cells. Although the planarian longitudinal muscles are already known to provide polarity cues for body plan reset during regeneration,[25,51] our data reveal another essential, more upstream function of the planarian muscles in facilitating the propagation of Erk waves and thereby coordinating wound responses across space and cell types.

A diffusive signaling relay model identifies key cell morphological properties required to accelerate signal propagation

We used a signaling relay model (Figures S6A–S6C)[53] to investigate morphological properties that may grant muscle cells special capacities in propagating Erk activity. Consistent with our intuition and analytical estimation (see STAR Methods), the numerical simulation showed that when intracellular propagation is much faster than extracellular propagation, wave speed increases with propagating cell size (Figure S6D). We then extended the model to consider heterogeneous tissues containing both long cells, the major cell type propagating the signal, and small round cells. We systematically tuned the length, volume density, and orientation of long cells, as well as the fraction of small cells that also can participate in the signal relay, to determine their effects on the speed of Erk activity waves (Figure S6E).

Through simulation, we found that the wave speed multiplied with increasing length of the long cells even in heterogeneous tissues (Figures 6A and S6E). This trend was robust to changes of other model parameters such as long cell density and molecular kinetics of Erk signaling (Figures S6F–S6H). Indeed, the wave speed $v \sim L\sqrt{aD}$, consistent with the prediction made by our analytical model omitting small non-propagating cells (see STAR Methods).

We further found that the wave speed was independent of long cell volume density in the low-density regime, but above the critical density ($\sim$0.2) where the long cells begin to form large continuous clusters (Figures S6I and S6J), the wave speed increased quickly with long cell density (Figure 6B). This transition implies that signal transmission via continuous paths formed by long cells connecting to each other and clustering in space is the major mode of wave propagation. In addition, the more cells that aligned with the direction of signal propagation, the faster the wave propagation was (Figures 6C and S6K). By contrast, the wave speed was only weakly dependent on the fraction of small cells that can also participate in the signal relay when the long cell density is low, and this dependence diminished with increasing long cell density (Figures 6D and S6L).

Whereas previous modeling efforts mostly focus on the effects of varying kinetics that control activation within individual cells and communication between adjacent cells,[37,43,53,54] our model reveals the contribution of large-scale structures formed by clusters of cells that collectively enhance the rate of signal propagation. Conceptually, our model conveys three important messages. First, to function as signaling superhighways, the propagating cells not only need to be long but also should form dense parallel tracks, which are exactly the obvious attributes of the planarian longitudinal body-wall muscles.[25] Second,

(B) Erk activity, measured by western blotting, vs. time post amputation in proximal (left) and distal (right) tissues from control RNAi (orange) and *myoD* RNAi (blue) animals. Each data point represents three biological replicates containing tissue fragments collected from ten animals.
(C) Heatmap showing the expression of example global response genes in proximal (PR) and distal (DS) tissues of control RNAi (left) and *myoD* RNAi (right) animals, measured from three biological replicates of five $\sim$5 mm long animals. Upregulation of these genes after injury requires Erk activation (Figure S1D). Erk-dependence in muscle cells was determined using the scRNA-seq data.
(D) Fold change of wound response genes at 6 hpa (p value < 0.001, two-sided Welch's t test, compared with 0 hpa, three biological replicates each containing five $\sim$5 mm long animals) in distal tissues of control RNAi and *myoD* RNAi animals. n.g., number of genes.
(E) Overlap of Erk-dependent (magenta) and *myoD*-dependent (blue) wound response genes in distal tissues. Numbers are percentage of genes within each sector.
(F) Double FISH showing wound response gene expression (magenta) in cells expressing cell-type-specific markers (green), i.e., *piwi-1*, neoblasts; *zpuf-6*, late epidermal progenitors; and *porcupine*, intestine, in distal regions (box in schematic) at 6 hpa, which is ablated by *myoD* RNAi.
(G) (Left) Representative images of anti-H3P staining showing that cell proliferation is reduced only in distal tissues after *myoD* RNAi. (Right) Number of $H3P^+$ cells counted in proximal (PR) and distal (DS) regions. Animals are pooled from two independent experiments. ***p < 0.001; NS: no significant difference, two-sided Welch's t test.
Error bars: standard derivation (SD) in (B), 95% confidence interval in (G); n in (F) and (G): number of samples consistent with the image out of the total number of samples analyzed. Scale bars: 20 μm in (A) and (F) and 500 μm in (G).
See also Figure S5 and Table S2.

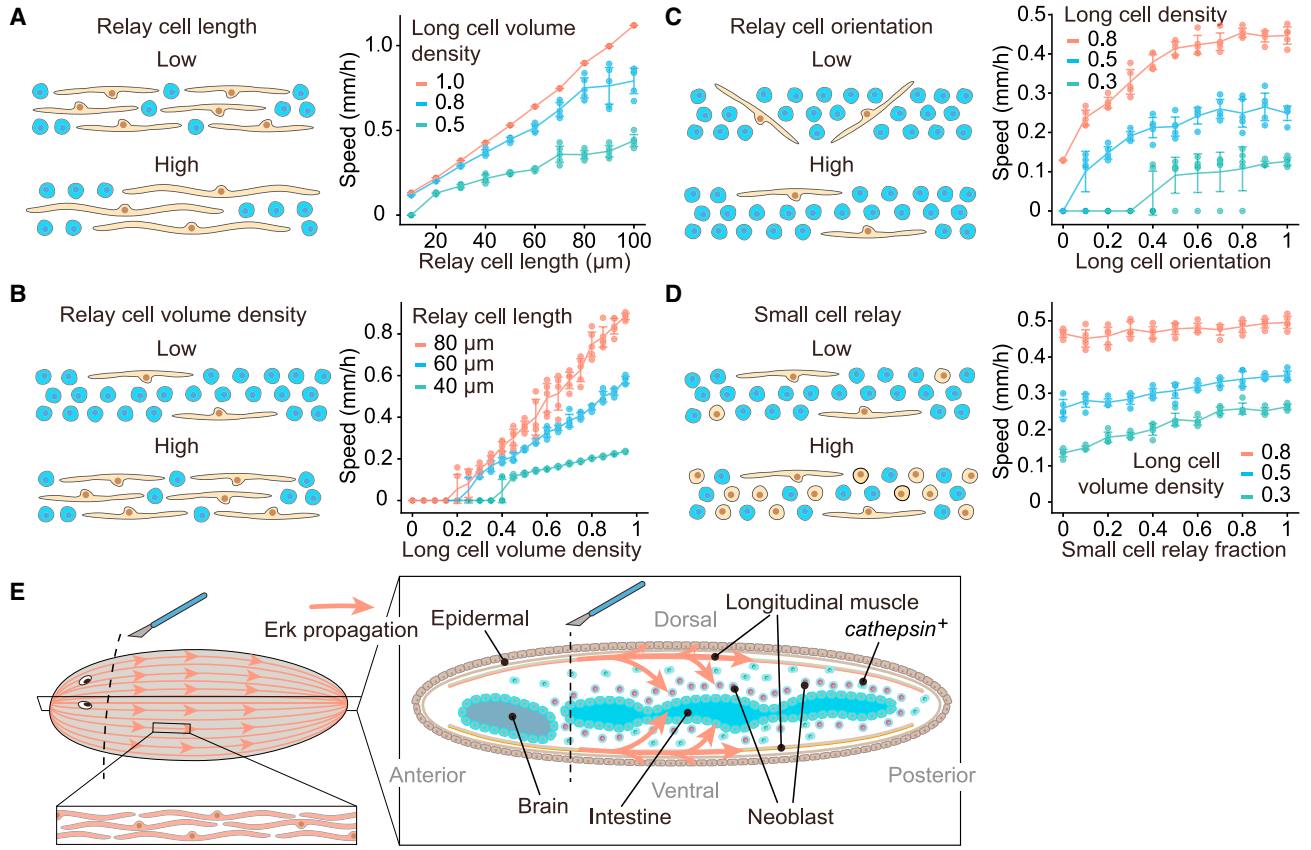

Figure 6. A diffusive relay model identifies cell morphological properties influencing signal propagation in heterogeneous tissues

(A) The speed of signal propagation increases with the length of relay cells.

(B) Signal propagation speed increases with long cell volume density.

(C) Signal propagation speed increases with the orientation factor of long cells, which is defined by the fraction of long cells extending along the wave direction whereas other long cells are perpendicular.

(D) Signal propagation speed is weakly dependent on the fraction of small cells that can relay the signal. Except for simulations in (C), long cells are assumed to be aligned with the wave propagation direction. In (A)–(C), small cells can only receive signal. In (C) and (D), long cells are 50 μm in length. In schematics, yellow: relay cells, blue: receiving cells. Error bars: standard derivation (SD) calculated from five simulations with long cells randomly positioned in the two-dimensional (2D) space.

(E) Model of the muscle cell function in propagating wound signals through Erk wave.

See also Figures S5 and S6.

in the presence of long cells, smaller cells may contribute minimally to signal propagation and get activated by signals from long cells. Strictly speaking, these small cells are activated in a "phase wave,"[33] which is distinct from but driven by the trigger wave traveling through the long cells. This mixed mode of propagation may be a signature of signaling in heterogeneous tissues. Finally, as our model has no architecture specific to the planarian tissues, its major conclusions may be generalizable to other complex and heterogeneous multicellular systems to predict the effects of cell morphology in determining signal propagation dynamics.

DISCUSSION

In this study, we revealed a mechanism for wound signals to traverse distances of several millimeters within just hours. We proposed the notion of pioneer cells—cells that lead in signal transduction (at least over long distances) and then relay the signal to other cell types. We argued that these pioneer cells need to have special morphological properties to act as superhighways for rapid signal propagation in heterogeneous tissues. In planarians, the longitudinal body-wall muscles play this role and are required to propagate the wound signal in the form of Erk waves and to activate responses in tissues distant to wounds (Figure 6E). To draw an analogy, these muscle cells function much like a circulatory system for disseminating wound signals across long distances[7,8]; however, no fluid flow is involved, instead, the biochemical signals propagate as a trigger wave through a diffusion-reaction-based mechanism.[33–36] The wave speed is unexpectedly fast for a multicellular system and roughly matches some intracellular waves in large cells.[39,40] In a way, the planarians respond to injury so rapidly as if they are gigantic unicellular organisms, though the signal propagation involves both intracellular and extracellular components.

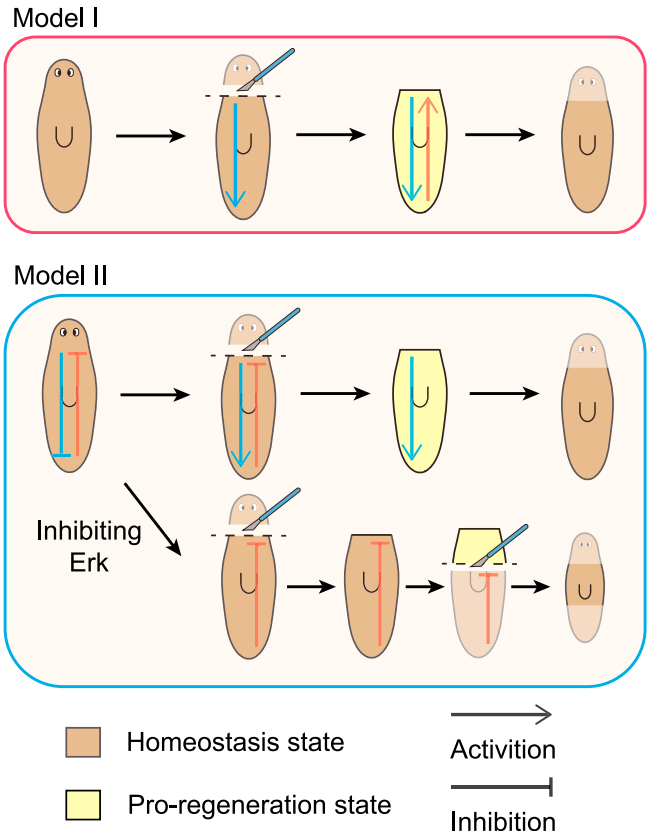

Figure 7. Models of feedback between proximal and distal tissues during regeneration

(Top) Model I: wound signal (blue) travels from proximal to distal. Then the distal tissue produces a secondary, activating signal (red) to the tissue at wounds to license regeneration. Yellow color indicates a pro-regeneration state. (Bottom) Model II: uninjured tissues produce inhibitory signals to block over-growth during homeostasis (blue and red). Inhibition is released when the wound signal travel through the body and the tissue enters a pro-regeneration state (yellow). When Erk activity propagation is inhibited, the distal tissue remains in an inhibitory state (red) causing regeneration to stall. A second amputation removes the inhibitory signal allowing the remaining tissue to enter the pro-regeneration state. Our data favors model II.

By perturbing Erk activity propagation, we provided strong evidence suggesting that DS wound responses are necessary for the current round of regeneration. Regeneration stalls without DS wound responses before the re-specification of anterior poles, an early event during regeneration.[55] In animals with Erk signal propagation blocked, amputating the DS tissues within the first few hours after the first injury is sufficient to rescue the regeneration deficiencies. Collectively, these observations reveal that the PR and DS wound responses should have distinct functions and must interact with each other to enable regeneration.

At PR sites, the injury-induced upregulation of a few previously characterized key regulators of the planarian regeneration, including *follistatin* (*fst*),[56–58] *notum*,[55] and *runt-1*,[24] is indeed Erk dependent.[28] Intriguingly, the injury-induced expression of *fst* and *notum* has been noted to be mostly in *myoD*$^{+}$ muscles facing wounds,[25] implicating a direct regulation of *fst* and *notum* transcription through the Erk pathway as a part of the PR wound responses. However, the function of DS wound responses may be independent of these known regulators, as their activation in DS tissues is not observed in our data. Although we showed that neoblast proliferation in DS tissues requires Erk activation, it is unlikely that regeneration relies on these cells as the source of new tissues. Removing the DS tissues, and the neoblasts therein, does not inhibit regeneration. Consistently, neoblast proliferation is sustained at wounds for up to a week during the planarian regeneration but is only transiently elevated in DS tissues.[6] The planarian regeneration also involves apoptosis[59] and remodeling of pre-existing tissues,[26] but these processes occur only at much later time points, i.e., a few days after injury.

We propose a model in which the DS wound responses act through providing feedback to the PR responses at wounds (Figure 7). It is possible that the planarian regeneration requires a secondary, activating signal provided by the DS tissues. Alternatively, uninjured tissues may produce inhibitory signals to block over-growth during homeostasis, but this inhibition is released when the wound signal arrives at DS tissues. This process triggers cells to switch from the homeostatic state to a pro-regeneration state and licenses the growth of new tissues. Our data favor the second scenario. The existence of activating signals in DS wound responses would imply that we have to supplement the specific cues to rescue the regeneration deficiencies caused by missing DS responses. This is not what we observed. Instead, amputating the DS tissues, which induces the PR wound responses, is sufficient to rescue the regeneration. Identifying the molecular basis of this feedback will be an important avenue of future research.

Limitations of the study

The lack of advanced transgenic and live imaging tools in planarians limits our ability to resolve the spatiotemporal dynamics of Erk activation. Although our western blotting protocol is quantitative and highly specific, it is tedious, requires large amounts of tissue as input, and only provides information at specific time snapshots. In these experiments, we used tissue fragments of ~1 mm in length, each should already take ~1 h for the Erk wave to travel through, even assuming an infinitely narrow wave front. This limitation in the spatial resolution led to the broadening of the measured Erk activity peaks in time. As planarian transgenic tools develop,[60] we expect that live imaging using genetically encoded Erk activity reporters should help to visualize the propagation of Erk waves with higher resolution and enable the precise measurement of kinetic parameters of the signaling pathway. This will allow us to validate the model predictions quantitatively. Finally, in addition to longitudinal muscles, planarian muscle cells also organize into a layer of circular fibers running along the medial-lateral (M-L) axis[25] and dorsal-ventral (D-V) fibers.[61] These muscle populations are specified through distinct pathways and play different functional roles in regeneration. As planarian bodies are narrow and flat, wound signal does not need to propagate through long distances along M-L or D-V axes. Whether Erk signals travel preferentially along longitudinal muscles and how these muscle populations respond to injury to adapt to the different functional needs remain to be determined.

STAR★METHODS

Detailed methods are provided in the online version of this paper and include the following:

- KEY RESOURCES TABLE
- RESOURCE AVAILABILITY
  - Lead contact
  - Materials availability
  - Data and code availability
- EXPERIMENTAL MODEL AND STUDY PARTICIPANT DETAILS
  - Animals
- METHOD DETAILS
  - Bulk RNAseq and data analysis
  - Single-cell RNAseq and data analysis
  - Western blotting
  - Cloning, *in situ* hybridization and immunostaining
  - RNAi and drug treatment
  - Experimental design
  - Working model and alternative hypotheses
  - Mathematical modeling
  - Numerical simulation
- QUANTIFICATION AND STATISTICAL ANALYSIS

SUPPLEMENTAL INFORMATION

Supplemental information can be found online at https://doi.org/10.1016/j.cell.2023.06.019.

ACKNOWLEDGMENTS

We thank L.E. O'Brien, S. Granick, S. Di Talia, Q. Yang, G. Maryu, M. Wu, G. Cao, K. Zhou, Z. Zeng, and members of Wang and Ferrell labs for critical discussions and J. Gibson, S. Sarkar, and E. Song for their technical assistance. Y.F. and X.Z. are Bio-X Stanford Interdisciplinary Graduate Fellows. C.C. is supported by an NSF Graduate Research Fellowship and a Stanford Graduate Fellowship. B.W. is a Beckman Young Investigator. This work is supported by NIH grant 1R35GM138061 to B.W. and 5R35GM131792 to J.E.F.

AUTHOR CONTRIBUTIONS

Conceptualization, Y.F., J.E.F., and B.W.; methodology, Y.F., C.C., P.L., and X.Z.; investigation, Y.F., C.C., P.L., and X.Z.; formal analysis, Y.F. and C.C.; validation, Y.F.; writing, Y.F., J.E.F., and B.W. with feedback from all other authors; funding acquisition, B.W. and J.E.F.; supervision, B.W.

DECLARATION OF INTERESTS

The authors declare no competing interests.

INCLUSION AND DIVERSITY

One or more of the authors of this paper self-identifies as an underrepresented ethnic minority in their field of research or within their geographical location.

Received: May 26, 2022
Revised: January 11, 2023
Accepted: June 23, 2023
Published: July 21, 2023

REFERENCES

1. Losner, J., Courtemanche, K., and Whited, J.L. (2021). A cross-species analysis of systemic mediators of repair and complex tissue regeneration. NPJ Regen. Med. *6*, 21. https://doi.org/10.1038/s41536-021-00130-6.
2. Kuris, A.M., and Mager, M. (1975). Effect of limb regeneration on size increase at molt of the shore crabs *Hemigrapsus oregonensis* and *Pachygrapsus crassipes*. J. Exp. Zool. *193*, 353–360. https://doi.org/10.1002/jez.1401930311.
3. Vethamany-Globus, S., and Liversage, R.A. (1973). The relationship between the anterior pituitary gland and the pancreas in tail regeneration of the adult newt. J. Embryol. Exp. Morphol. *30*, 415–426. https://doi.org/10.1242/dev.30.2.415.
4. Kranz, D., Hecht, A., and Fuhrmann, I. (1976). The influence of hyperthyroidism and hypothyroidism on the wound healing of experimental myocardial infarction in the rat. Exp. Pathol. *12*, 129–136. https://doi.org/10.1016/s0014-4908(76)80035-x.
5. Ricci, L., and Srivastava, M. (2018). Wound-induced cell proliferation during animal regeneration. Wiley Interdiscip. Rev. Dev. Biol. *7*, e321. https://doi.org/10.1002/wdev.321.
6. Wenemoser, D., and Reddien, P.W. (2010). Planarian regeneration involves distinct stem cell responses to wounds and tissue absence. Dev. Biol. *344*, 979–991. https://doi.org/10.1016/j.ydbio.2010.06.017.
7. Rodgers, J.T., King, K.Y., Brett, J.O., Cromie, M.J., Charville, G.W., Maguire, K.K., Brunson, C., Mastey, N., Liu, L., Tsai, C.R., et al. (2014). MTORC1 controls the adaptive transition of quiescent stem cells from G0 to GAlert. Nature *510*, 393–396. https://doi.org/10.1038/nature13255.
8. Rodgers, J.T., Schroeder, M.D., Ma, C., and Rando, T.A. (2017). HGFA is an injury-regulated systemic factor that induces the transition of stem cells into GAlert. Cell Rep. *19*, 479–486. https://doi.org/10.1016/j.celrep.2017.03.066.
9. Johnson, K., Bateman, J., DiTommaso, T., Wong, A.Y., and Whited, J.L. (2018). Systemic cell cycle activation is induced following complex tissue injury in axolotl. Dev. Biol. *433*, 461–472. https://doi.org/10.1016/j.ydbio.2017.07.010.
10. Payzin-Dogru, D., Wilson, S.E., Blair, S.J., Erdogan, B., Hossain, S., Cammarata, L., Velazquez Matos, J., and Whited, J.L. (2021). Nerve-mediated amputation-induced stem cell activation primes distant appendages for future regeneration events in axolotl. https://doi.org/10.1101/2021.12.29.474455.
11. Sun, F., Ou, J., Shoffner, A.R., Luan, Y., Yang, H., Song, L., Safi, A., Cao, J., Yue, F., Crawford, G.E., et al. (2022). Enhancer selection dictates gene expression responses in remote organs during tissue regeneration. Nat. Cell Biol. *24*, 685–696. https://doi.org/10.1038/s41556-022-00906-y.
12. Halme, A., Cheng, M., and Hariharan, I.K. (2010). Retinoids regulate a developmental checkpoint for tissue regeneration in *Drosophila*. Curr. Biol. *20*, 458–463. https://doi.org/10.1016/j.cub.2010.01.038.
13. Hirose, K., Payumo, A.Y., Cutie, S., Hoang, A., Zhang, H., Guyot, R., Lunn, D., Bigley, R.B., Yu, H., Wang, J., et al. (2019). Evidence for hormonal control of heart regenerative capacity during endothermy acquisition. Science *364*, 184–188. https://doi.org/10.1126/science.aar2038.
14. Kikuchi, K., Holdway, J.E., Major, R.J., Blum, N., Dahn, R.D., Begemann, G., and Poss, K.D. (2011). Retinoic acid production by endocardium and epicardium is an injury response essential for zebrafish heart regeneration. Dev. Cell *20*, 397–404. https://doi.org/10.1016/j.devcel.2011.01.010.
15. Hasegawa, T., Nakajima, T., Ishida, T., Kudo, A., and Kawakami, A. (2015). A diffusible signal derived from hematopoietic cells supports the survival and proliferation of regenerative cells during zebrafish fin fold regeneration. Dev. Biol. *399*, 80–90. https://doi.org/10.1016/j.ydbio.2014.12.015.
16. Chera, S., Ghila, L., Dobretz, K., Wenger, Y., Bauer, C., Buzgariu, W., Martinou, J.C., and Galliot, B. (2009). Apoptotic cells provide an unexpected source of Wnt3 signaling to drive *Hydra* head regeneration. Dev. Cell *17*, 279–289. https://doi.org/10.1016/j.devcel.2009.07.014.

17. Müller, P., Rogers, K.W., Yu, S.R., Brand, M., and Schier, A.F. (2013). Morphogen transport. Development *140*, 1621–1638. https://doi.org/10.1242/dev.083519.

18. Hiratsuka, T., Fujita, Y., Naoki, H., Aoki, K., Kamioka, Y., and Matsuda, M. (2015). Intercellular propagation of extracellular signal-regulated kinase activation revealed by in vivo imaging of mouse skin. eLife *4*, e05178. https://doi.org/10.7554/eLife.05178.

19. De Simone, A., Evanitsky, M.N., Hayden, L., Cox, B.D., Wang, J., Tornini, V.A., Ou, J., Chao, A., Poss, K.D., and Di Talia, S. (2021). Control of osteoblast regeneration by a train of Erk activity waves. Nature *590*, 129–133. https://doi.org/10.1038/s41586-020-03085-8.

20. Aoki, K., Kondo, Y., Naoki, H., Hiratsuka, T., Itoh, R.E., and Matsuda, M. (2017). Propagating wave of ERK activation orients collective cell migration. Dev. Cell *43*, 305–317.e5. https://doi.org/10.1016/j.devcel.2017.10.016.

21. Newmark, P.A., and Sánchez Alvarado, A. (2002). Not your father's planarian: A classic model enters the era of functional genomics. Nat. Rev. Genet. *3*, 210–219. https://doi.org/10.1038/nrg759.

22. Rink, J.C. (2013). Stem cell systems and regeneration in planaria. Dev. Genes Evol. *223*, 67–84. https://doi.org/10.1007/s00427-012-0426-4.

23. Reddien, P.W. (2018). The cellular and molecular basis for planarian regeneration. Cell *175*, 327–345. https://doi.org/10.1016/j.cell.2018.09.021.

24. Wenemoser, D., Lapan, S.W., Wilkinson, A.W., Bell, G.W., and Reddien, P.W. (2012). A molecular wound response program associated with regeneration initiation in planarians. Genes Dev. *26*, 988–1002. https://doi.org/10.1101/gad.187377.112.

25. Scimone, M.L., Cote, L.E., and Reddien, P.W. (2017). Orthogonal muscle fibres have different instructive roles in planarian regeneration. Nature *551*, 623–628. https://doi.org/10.1038/nature24660.

26. Benham-Pyle, B.W., Brewster, C.E., Kent, A.M., Mann, F.G., Chen, S., Scott, A.R., Box, A.C., and Sánchez Alvarado, A. (2021). Identification of rare, transient post-mitotic cell states that are induced by injury and required for whole-body regeneration in *Schmidtea mediterranea*. Nat. Cell Biol. *23*, 939–952. https://doi.org/10.1038/s41556-021-00734-6.

27. Tasaki, J., Shibata, N., Nishimura, O., Itomi, K., Tabata, Y., Son, F., Suzuki, N., Araki, R., Abe, M., Agata, K., et al. (2011). ERK signaling controls blastema cell differentiation during planarian regeneration. Development *138*, 2417–2427. https://doi.org/10.1242/dev.060764.

28. Owlarn, S., Klenner, F., Schmidt, D., Rabert, F., Tomasso, A., Reuter, H., Mulaw, M.A., Moritz, S., Gentile, L., Weidinger, G., et al. (2017). Generic wound signals initiate regeneration in missing-tissue contexts. Nat. Commun. *8*, 2282. https://doi.org/10.1038/s41467-017-02338-x.

29. Srivastava, M. (2021). Beyond casual resemblance: rigorous frameworks for comparing regeneration across species. Annu. Rev. Cell Dev. Biol. *37*, 415–440. https://doi.org/10.1146/annurev-cellbio-120319-114716.

30. Mace, K.A., Pearson, J.C., and McGinnis, W. (2005). An epidermal barrier wound repair pathway in *Drosophila* is mediated by grainy head. Science *308*, 381–385. https://doi.org/10.1126/science.1107573.

31. DuBuc, T.Q., Traylor-Knowles, N., and Martindale, M.Q. (2014). Initiating a regenerative response; cellular and molecular features of wound healing in the cnidarian *Nematostella vectensis*. BMC Biol. *12*, 24. https://doi.org/10.1186/1741-7007-12-24.

32. Tursch, A., Bartsch, N., Mercker, M., Schlüter, J., Lommel, M., Marciniak-Czochra, A., Özbek, S., and Holstein, T.W. (2022). Injury-induced MAPK activation triggers body axis formation in *Hydra* by default Wnt signaling. Proc. Natl. Acad. Sci. USA *119*, e2204122119. https://doi.org/10.1073/pnas.2204122119.

33. Winfree, A.T. (1974). Two kinds of wave in an oscillating chemical solution. Faraday Symp. Chem. Soc. *9*, 38–46. https://doi.org/10.1039/FS9740900038.

34. Tyson, J.J., and Keener, J.P. (1988). Singular perturbation theory of traveling waves in excitable media (a review). Phys. D *32*, 327–361. https://doi.org/10.1016/0167-2789(88)90062-0.

35. Gelens, L., Anderson, G.A., and Ferrell, J.E. (2014). Spatial trigger waves: positive feedback gets you a long way. Mol. Biol. Cell *25*, 3486–3493. https://doi.org/10.1091/mbc.E14-08-1306.

36. Deneke, V.E., and Di Talia, S. (2018). Chemical waves in cell and developmental biology. J. Cell Biol. *217*, 1193–1204. https://doi.org/10.1083/jcb.201701158.

37. Hayden, L.D., Poss, K.D., De Simone, A., and Di Talia, S. (2021). Mathematical modeling of Erk activity waves in regenerating zebrafish scales. Biophys. J. *120*, 4287–4297. https://doi.org/10.1016/j.bpj.2021.05.004.

38. Gagliardi, P.A., Dobrzyński, M., Jacques, M.A., Dessauges, C., Ender, P., Blum, Y., Hughes, R.M., Cohen, A.R., and Pertz, O. (2021). Collective ERK/Akt activity waves orchestrate epithelial homeostasis by driving apoptosis-induced survival. Dev. Cell *56*, 1712–1726.e6. https://doi.org/10.1016/j.devcel.2021.05.007.

39. Chang, J.B., and Ferrell, J.E. (2013). Mitotic trigger waves and the spatial coordination of the *Xenopus* cell cycle. Nature *500*, 603–607. https://doi.org/10.1038/nature12321.

40. Cheng, X., and Ferrell, J.E. (2018). Apoptosis propagates through the cytoplasm as trigger waves. Science *361*, 607–612. https://doi.org/10.1126/science.aah4065.

41. Cohen-Saidon, C., Cohen, A.A., Sigal, A., Liron, Y., and Alon, U. (2009). Dynamics and variability of ERK2 response to EGF in individual living cells. Mol. Cell *36*, 885–893. https://doi.org/10.1016/j.molcel.2009.11.025.

42. Regot, S., Hughey, J.J., Bajar, B.T., Carrasco, S., and Covert, M.W. (2014). High-sensitivity measurements of multiple kinase activities in live single cells. Cell *157*, 1724–1734. https://doi.org/10.1016/j.cell.2014.04.039.

43. Aoki, K., Kumagai, Y., Sakurai, A., Komatsu, N., Fujita, Y., Shionyu, C., and Matsuda, M. (2013). Stochastic ERK activation induced by noise and cell-to-cell propagation regulates cell density-dependent proliferation. Mol. Cell *52*, 529–540. https://doi.org/10.1016/j.molcel.2013.09.015.

44. Nakamura, A., Goto, Y., Kondo, Y., and Aoki, K. (2021). Shedding light on developmental ERK signaling with genetically encoded biosensors. Development *148*, dev199767. https://doi.org/10.1242/dev.199767.

45. Duchesne, L., Octeau, V., Bearon, R.N., Beckett, A., Prior, I.A., Lounis, B., and Fernig, D.G. (2012). Transport of fibroblast growth factor 2 in the pericellular matrix is controlled by the spatial distribution of its binding sites in heparan sulfate. PLoS Biol. *10*, e1001361. https://doi.org/10.1371/journal.pbio.1001361.

46. Venero Galanternik, M., Kramer, K.L., and Piotrowski, T. (2015). Heparan sulfate proteoglycans regulate Fgf signaling and cell polarity during collective cell migration. Cell Rep. *10*, 414–428. https://doi.org/10.1016/j.celrep.2014.12.043.

47. Verveer, P.J., Wouters, F.S., Reynolds, A.R., and Bastiaens, P.I.H. (2000). Quantitative imaging of lateral ErbB1 receptor signal propagation in the plasma membrane. Science *290*, 1567–1570. https://doi.org/10.1126/science.290.5496.1567.

48. Reynolds, A.R., Tischer, C., Verveer, P.J., Rocks, O., and Bastiaens, P.I.H. (2003). EGFR activation coupled to inhibition of tyrosine phosphatases causes lateral signal propagation. Nat. Cell Biol. *5*, 447–453. https://doi.org/10.1038/ncb981.

49. Das, J., Ho, M., Zikherman, J., Govern, C., Yang, M., Weiss, A., Chakraborty, A.K., and Roose, J.P. (2009). Digital signaling and hysteresis characterize ras activation in lymphoid cells. Cell *136*, 337–351. https://doi.org/10.1016/j.cell.2008.11.051.

50. Fisher, R.A. (1937). The wave of advance of advantageous genes. Ann. Eugen. *7*, 355–369. https://doi.org/10.1111/j.1469-1809.1937.tb02153.x.

51. Witchley, J.N., Mayer, M., Wagner, D.E., Owen, J.H., and Reddien, P.W. (2013). Muscle cells provide instructions for planarian regeneration. Cell Rep. *4*, 633–641. https://doi.org/10.1016/j.celrep.2013.07.022.

52. Lim, Y., Khariton, M., Lane, K., Shiver, A., Ng, K., Bray, S., Qin, J., Huang, K.C., and Wang, B. (2019). Mechanically resolved imaging of bacteria using expansion microscopy. PLoS Biol. *17*, e3000268. https://doi.org/10.1101/622654.

53. Dieterle, P.B., Min, J., Irimia, D., and Amir, A. (2020). Dynamics of diffusive cell signaling relays. eLife *9*, e61771. https://doi.org/10.7554/eLife.61771.

54. Yde, P., Mengel, B., Jensen, M.H., Krishna, S., and Trusina, A. (2011). Modeling the NF-κB mediated inflammatory response predicts cytokine waves in tissue. BMC Syst. Biol. *5*, 115. https://doi.org/10.1186/1752-0509-5-115.

55. Petersen, C.P., and Reddien, P.W. (2011). Polarized notum activation at wounds inhibits Wnt function to promote planarian head regeneration. Science *332*, 852–855. https://doi.org/10.1126/science.1202143.

56. Roberts-Galbraith, R.H., and Newmark, P.A. (2013). Follistatin antagonizes activin signaling and acts with Notum to direct planarian head regeneration. Proc. Natl. Acad. Sci. USA *110*, 1363–1368. https://doi.org/10.1073/pnas.1214053110.

57. Gaviño, M.A., Wenemoser, D., Wang, I.E., and Reddien, P.W. (2013). Tissue absence initiates regeneration through follistatin-mediated inhibition of activin signaling. eLife *2*, e00247. https://doi.org/10.7554/eLife.00247.

58. Tewari, A.G., Stern, S.R., Oderberg, I.M., and Reddien, P.W. (2018). Cellular and molecular responses unique to major injury are dispensable for planarian regeneration. Cell Rep. *25*, 2577–2590.e3. https://doi.org/10.1016/j.celrep.2018.11.004.

59. Pellettieri, J., Fitzgerald, P., Watanabe, S., Mancuso, J., Green, D.R., and Sánchez Alvarado, A. (2010). Cell death and tissue remodeling in planarian regeneration. Dev. Biol. *338*, 76–85. https://doi.org/10.1016/j.ydbio.2009.09.015.

60. Hall, R.N., Weill, U., Drees, L., Leal-Ortiz, S., Li, H., Khariton, M., Chai, C., Xue, Y., Rosental, B., Quake, S.R., et al. (2022). Heterologous reporter expression in the planarian *Schmidtea mediterranea* through somatic mRNA transfection. Cell Rep. Methods *2*, 100298. https://doi.org/10.1016/j.crmeth.2022.100298.

61. Scimone, M.L., Wurtzel, O., Malecek, K., Fincher, C.T., Oderberg, I.M., Kravarik, K.M., and Reddien, P.W. (2018). foxF-1 controls specification of non-body wall muscle and phagocytic cells in planarians. Curr. Biol. *28*, 3787–3801.e6. https://doi.org/10.1016/j.cub.2018.10.030.

62. Newmark, P.A., and Sánchez Alvarado, A. (2000). Bromodeoxyuridine specifically labels the regenerative stem cells of planarians. Dev. Biol. *220*, 142–153. https://doi.org/10.1006/dbio.2000.9645.

63. Guo, L., Zhang, S., Rubinstein, B., Ross, E., and Alvarado, A.S. (2016). Widespread maintenance of genome heterozygosity in *Schmidtea mediterranea*. Nat. Ecol. Evol. *1*, 19. https://doi.org/10.1038/s41559-016-0019.

64. Collins, J.J., Hou, X., Romanova, E.V., Lambrus, B.G., Miller, C.M., Saberi, A., Sweedler, J.V., and Newmark, P.A. (2010). Genome-wide analyses reveal a role for peptide hormones in planarian germline development. PLoS Biol. *8*, e1000509. https://doi.org/10.1371/journal.pbio.1000509.

65. Langmead, B., and Salzberg, S.L. (2012). Fast gapped-read alignment with Bowtie 2. Nat. Methods *9*, 357–359. https://doi.org/10.1038/nmeth.1923.

66. Love, M.I., Huber, W., and Anders, S. (2014). Moderated estimation of fold change and dispersion for RNA-seq data with DESeq2. Genome Biol. *15*, 550. https://doi.org/10.1186/s13059-014-0550-8.

67. Smith, T., Heger, A., and Sudbery, I. (2017). UMI-tools: modeling sequencing errors in Unique Molecular Identifiers to improve quantification accuracy. Genome Res. *27*, 491–499. https://doi.org/10.1101/gr.209601.116.

68. Martin, M. (2011). Cutadapt removes adapter sequences from high-throughput sequencing reads. EMBnet J. *17*, 10–12. https://doi.org/10.14806/ej.17.1.200.

69. Polański, K., Young, M.D., Miao, Z., Meyer, K.B., Teichmann, S.A., and Park, J.E. (2020). BBKNN: fast batch alignment of single cell transcriptomes. Bioinformatics *36*, 964–965. https://doi.org/10.1093/bioinformatics/btz625.

70. Tarashansky, A.J., Xue, Y., Li, P., Quake, S.R., and Wang, B. (2019). Self-assembling manifolds in single-cell RNA sequencing data. eLife *8*, e48994. https://doi.org/10.7554/eLife.48994.

71. Rozanski, A., Moon, H., Brandl, H., Martín-Durán, J.M., Grohme, M.A., Hüttner, K., Bartscherer, K., Henry, I., and Rink, J.C. (2019). PlanMine 3.0—improvements to a mineable resource of flatworm biology and biodiversity. Nucleic Acids Res. *47*, D812–D820. https://doi.org/10.1093/nar/gky1070.

72. Fincher, C.T., Wurtzel, O., de Hoog, T., Kravarik, K.M., and Reddien, P.W. (2018). Cell type transcriptome atlas for the planarian *Schmidtea mediterranea*. Science *360*, eaaq1736. https://doi.org/10.1126/science.aaq1736.

73. Stückemann, T., Cleland, J.P., Werner, S., Thi-Kim Vu, H., Bayersdorf, R., Liu, S.Y., Friedrich, B., Jülicher, F., and Rink, J.C. (2017). Antagonistic self-organizing patterning systems control maintenance and regeneration of the anteroposterior axis in planarians. Dev. Cell *40*, 248–263.e4. https://doi.org/10.1016/j.devcel.2016.12.024.

74. King, R.S., and Newmark, P.A. (2013). In situ hybridization protocol for enhanced detection of gene expression in the planarian *Schmidtea mediterranea*. BMC Dev. Biol. *13*, 8. https://doi.org/10.1186/1471-213X-13-8.

75. Ogura, Y., Wen, F.-L., Sami, M.M., Shibata, T., and Hayashi, S. (2018). A switch-like activation relay of EGFR-ERK signaling regulates a wave of cellular contractility for epithelial invagination. Dev. Cell *46*, 162–172.e5. https://doi.org/10.1016/j.devcel.2018.06.004.

76. Shvartsman, S.Y., Hagan, M.P., Yacoub, A., Dent, P., Wiley, H.S., and Lauffenburger, D.A. (2002). Autocrine loops with positive feedback enable context-dependent cell signaling. Am. J. Physiol. Cell Physiol. *282*, C545–C559. https://doi.org/10.1152/ajpcell.00260.2001.

77. Luther, R. (1906). Raumliche fortplanzung chimischer Reaktionen. Z. Elektrotech. Elektrochem. *12*, 596–600.

78. Umesono, Y., Tasaki, J., Nishimura, Y., Hrouda, M., Kawaguchi, E., Yazawa, S., Nishimura, O., Hosoda, K., Inoue, T., and Agata, K. (2013). The molecular logic for planarian regeneration along the anterior-posterior axis. Nature *500*, 73–76. https://doi.org/10.1038/nature12359.

STAR★METHODS

KEY RESOURCES TABLE

REAGENT or RESOURCE	SOURCE	IDENTIFIER
Antibodies		
Anti-Digoxigenin-POD	Roche	11207733910; RRID: AB_514500
Anti-Dinitrophenyl	Vector Laboratories	SP-0603-1; RRID: AB_2336117
Anti-Digoxigenin-AP	Roche	11093274910; RRID: AB_514497
Anti-pErk	Santa Cruz Biotech	Sc-7383; RRID: AB_627545
Anti-Erk1/2	Cell Signaling	9102L; RRID: AB_330744
Anti-actin	Hybridoma Bank	JLA20; RRID: AB_528068
Goat anti-mouse IgG2a	LI-COR	926-32351; RRID: AB_2782998
Goat anti-rabbit IgG	Biotium	20067; RRID: AB_10871686
Goat anti-mouse IgM	Biotium	20485
Peroxidase goat anti-mouse IgG+IgM	Jackson ImmunoResearch	115-035-044; RRID: AB_2338503
Peroxidase goat anti-rabbit IgG (H+L)	Jackson ImmunoResearch	111-035-003; RRID: AB_2313567
Anti-phospho-Histone H3	Millipore	04-817; RRID: AB_1163440
2G3-3D7	DSHB	RRID: AB_2721943
Chemicals, peptides, and recombinant proteins		
Digoxigenin-11-UTP	Roche	11209256910
Dinitrophenyl-11-UTP	Perkin Elmer	NEL555001EA
Sodium azide	Thermo Fisher Scientific	014314-22
TRIzol Reagent	Thermo Fisher Scientific	15596026
Dimethyl sulfoxide (DMSO)	Fisher Scientific	D1391
U0126	Cell Signaling	9903S
Hoechst 33342	Thermo Fisher Scientific	H3570
Propodium iodide (PI)	Thermo Fisher Scientific	P3566
DAPI	Millipore Sigma	D9542
RNasin ribonuclease inhibitor	Promega	N2515
FAST SYBR Green Master Mix	Bio-rad	1725122
Zinc chloride	Millipore Sigma	Z0152
Dithiothreitol (DTT)	Thermo Fisher Scientific	R0861
Sodium Dodecyl Sulfate (SDS)	Fisher Scientific	BP166
cOmplete protease inhibitor	Millipore Sigma	5892791001
PhosSTOP	Millipore Sigma	4906845001
Benzonase	Millipore Sigma	E1014
NuPAGE 4 to 12% Bis-Tris gel	Invitrogen	NP0322BOX
NuPAGE MOPS running buffer	Invitrogen	NP0001
NuPAGE transfer buffer	Invitrogen	NP00061
Nitrocellulose membrane	Invitrogen	927-60001
Western blocking buffer	LI-COR	927-60001
Tween 20	Millipore Sigma	11332465001
RNase-free DNase	Promega	M6101
Ammonium acetate	Millipore Sigma	A7330
N-Acetyl-L-cysteine	Millipore Sigma	A7250
16% Formaldehyde	Thermo Fisher Scientific	PI28908
Nonidet P 40 substitute (NP-40)	Millipore Sigma	74385
Hydrogen peroxide solution	Millipore Sigma	H1009

(*Continued on next page*)

Continued		
REAGENT or RESOURCE	SOURCE	IDENTIFIER
Formamide	Roche	11814320001
Triton X-100	Thermo Fisher Scientific	BP151-500
Proteinase K solution	Thermo Fisher Scientific	25-530-049
Bovine serum albumin (BSA)	Jackson ImmunoResearch	001-000-161
Liberase TH	Millipore Sigma	5401151001
Critical commercial assays		
RNeasy Mini Kit	Qiagen	74104
Universal Plus mRNA-seq Library Preparation Kit	TECAN	0520-A01
Chromium Single Cell v3.1 Library/Gel Bead Kit	10x Genomics	1000121
Deposited data		
Bulk RNAseq	Sequence Read Archive	PRJNA894230
Single-cell RNAseq	Sequence Read Archive	PRJNA894242
Experimental models: organisms/strains		
Asexual *S. mediterranea* (strain CIW4)	Newmark and Sánchez Alvarado[62]	N/A
Sexual S2F8b planarian strain	Guo et al.[63]	N/A
Oligonucleotides		
Forward and reverse primers for riboprobe and dsRNA synthesis	This paper, Table S1	N/A
Vector pJC53.2	Collins et al.[64]	Addgene 26536
Software and algorithms		
Bowtie2	Langmead and Salzberg[65]	https://bowtie-bio.sourceforge.net
DESeq2	Love et al.[66]	https://bioconductor.org/
UMI-Tools	Smith et al.[67]	https://github.com/CGATOxford/UMI-tools
Cutadapt	Martin et al.[68]	https://cutadapt.readthedocs.io
BBKNN	Polański et al.[69]	https://github.com/Teichlab/bbknn
SAM	Tarashansky et al.[70]	https://github.com/atarashansky/self-assembling-manifold
Fiji	N/A	http://fiji.sc/
Python 3	N/A	http://www.python.org

RESOURCE AVAILABILITY

Lead contact

Further information and requests for all resources and reagents in this study should be directed to and will be fulfilled by the lead contact, Bo Wang (wangbo@stanford.edu).

Materials availability

This study did not generate new unique reagents.

Data and code availability

- Raw and processed bulk and single-cell RNAseq datasets generated for this study are available from NCBI BioProject with accession numbers PRJNA894230 (bulk RNAseq) and PRJNA894242 (single-cell RNAseq). Contig numbers for all mentioned genes are listed in Table S2.
- The diffusive signaling relay model is implemented in Python (version 3.7.12) and the code is available at https://github.com/fyh1221/Erk_wave_2022.
- Any additional information required to reanalyze the data reported in this work paper is available from the lead contact upon request.

EXPERIMENTAL MODEL AND STUDY PARTICIPANT DETAILS

Animals

Asexual *S. mediterranea* (CIW4) were maintained in the dark at 20 °C in 0.5 g/L Instant Ocean Sea Salts supplemented with 0.1 g/L sodium bicarbonate. Sexual planarians were maintained in 0.75× Montjuïc salts. They were fed calf liver paste once or twice a week and starved for 7 days before all experiments. Asexual animals of ~5 mm in length or sexuals of ~1 cm in length were used for western blotting experiments.

METHOD DETAILS

Bulk RNAseq and data analysis

We performed RNAseq on animals amputated at 1, 6 and 24 hpa. These time points were chosen based on previous studies showing that, at 1 hpa, wound responses should be already activated, at least in proximal tissues[24]; by 6 hpa, injury induced stem cell proliferation should occur in distal tissues[6]; and starting at 24 hpa, expression of position-control genes should be reestablished.[23]

In this experiment, tissue pieces were immediately frozen in Trizol at specific time points. Total RNA was then extracted from five pooled planarian fragments for each sample. Three biological replicates for each condition were processed in parallel. Libraries were prepared using the Universal Plus mRNA-seq Library Preparation Kit (TECAN), and sequenced on an Illumina NextSeq platform. Reads were mapped to the dd_Smed_v6 transcriptome (http://planmine.mpi-cbg.de)[71] using bowtie2 with –sensitive flag.[65] The raw read counts from different isoforms of the same gene were lumped for downstream analysis. Pairwise differential expression analysis was performed using DESeq2.[66] Heatmaps were generated using seaborn library with default parameters by calculating z-scores of normalized read counts generated by DESeq2.

Single-cell RNAseq and data analysis

Planarians were treated with either 0.25% DMSO or 25 μM U0126 in Instant Ocean for 24 h to fully block Erk activation (Figure S4A).[28] To enrich for wound-responding cells, animals were cut into three pieces 3 h before dissociation. To dissociate animals, planarians were finely minced with a razor blade. The minced tissues were then suspended in 3 mL of CMF (Ca/Mg-Free media: NaH_2PO_4 480 mg/L, NaCl 960 mg/L, KCl 1.44 g/L, $NaHCO_3$ 960 mg/L, HEPES 3.57 g/L, D-glucose 0.24 g/L, BSA 1 g/L, pH 7.4 in MilliQ H_2O) supplemented with equal volumes of DMSO or 25 μM U0126 in DMSO for the control and Erk-inhibited groups respectively, and rocked for a total of 10 min, with gentle pipetting every 3 min. The cell suspension was serially filtered through 100, 70, 40, 30-μm mesh strainers to remove undissociated tissue chunks and cell aggregates. The filtered cell suspensions were centrifuged at 400 g for 5 min, and resuspended in 2 mL of CMF supplemented with DMSO or U0126. The cells were then incubated in Hoechst (10 μg/mL) for 30 min in the dark and propidium iodide (2 μg/mL) afterwards. Cells were sorted on a SONY SH800S based on live-dead gating into CMF containing 1% BSA.

Sorted cells were spun down at 500 g for 5 min and resuspended in CMF with 1% BSA to a final density of ~1,000 cells per μL. Cells were then processed using 10x Genomics Chromium Controller and Chromium single cell v3.1 library/Gel Bead Kit. Amplified cDNA libraries were quantified using a bioanalyzer, and sequenced using Illumina Novaseq S4, generating in mean coverage of ~ 34,000 and ~31,000 read pairs per cell for the DMSO and U0126 treated cells, respectively. Sequenced reads were tagged with cell and molecular specific barcodes using UMI-tools,[67] trimmed of primer and polyA sequences using cutadapt,[68] and aligned to dd_Smed_v6[71] using bowtie2 –sensitive parameter.[65]

Downstream preprocessing and analysis were performed using UMI counts, for which we lumped raw counts from different isoforms of the same gene. Cells with fewer than 600 genes detected were filtered out, resulting in a final count of 13,276 and 14,793 cells for DMSO and U0126 treated samples. For each cell, we detected 2,252 genes and 6,483 UMI on average for the DMSO-treated sample and 2,275 genes and 6,043 UMI for the U0126-treated sample.

We normalized raw counts for sequencing coverage such that each cell has a total count equal to that of the median library size for all cells. The resulting counts were then added with a pseudo count of 1 and log-2 transformed. Integration of the control and Erk-inhibitor treated samples were performed using ridge regression on both technical effect and biological condition via BBKNN.[69] 2D embedding was performed using the SAM algorithm[70] with default parameters. Cells were annotated using cell-type specific markers from previously published RNAseq cell type atlas (Figure S2).[72] All annotations are provided in Table S3. *p*-values on gene expression differences in cells treated with DMSO and U1026 were performed on each cell type separately via Mann-Whitney-Wilcoxon test in sciPy library with default parameters.

Western blotting

At specified time points after amputation, animals were incubated in zinc fixative (100 nM $ZnCl_2$ in ethanol) for 45 min at 4 °C, then cut into four pieces along anterior-posterior axis, each measuring ~1 mm in length, on cool packs (Figure S4B). The most anterior tissue piece (P1) around the wound and the distal tissue piece (P3) between the pharynx and tail were used in U0126-treatment and *myoD* RNAi experiments because they exhibited largest dynamic ranges of Erk activity post amputation (Figure 2B). From the same proximal-distal position, ten tissue pieces were pooled per experiment and lysed by mechanical pestle homogenization in urea lysis buffer (6 M urea, 2% SDS, 130 mM DTT, 3.5 U/ml Benzonase, 1× protease inhibitor cocktail, 1× phosphatase inhibitor)

per experiment as described before.[73] Protein concentrations were determined by a Nanodrop spectrophotometer based on absorbance at 280 nm.

Western blotting was performed following an established protocol.[73] Briefly, samples were run in NuPAGE 4 to 12% Bis-Tris gels in NuPAGE MOPS running buffer, transferred onto nitrocellulose membranes in NuPAGE transfer buffer, blocked in Western blocking buffer for 1 h at room temperature and then incubated with primary antibodies overnight at 4 °C. Membranes were washed three times with washing buffer (PBS with 0.1% Tween 20) and then incubated with secondary antibodies for 1 h at room temperature. Membranes were washed again for three times with washing buffer, followed by washes with PBS, then dried and imaged on a LI-COR Odyssey imager.

Anti-pErk (1:1000), anti-Erk (1:250), and anti-actin (1:7500) were used as primary antibodies. The specificity of these Erk antibodies was validated by U0126 treatment and *erk* RNAi (Figure S4A). Goat anti-mouse IgG2a (1:10000), Goat anti-rabbit IgG (1:20000), and Goat anti-mouse IgM (1:10000) were used as secondary antibodies.

Cloning, *in situ* hybridization and immunostaining

Gene fragments were amplified from cDNA using oligonucleotide primers listed in Table S1 and cloned into the vector pJC53.2 (Addgene Plasmid ID: 26536).[64] RNA probes containing either Digoxigenin-11-UTP or Dinitrophenyl-11-UTP were synthesized using *in vitro* transcription. The products were treated with RNase-free DNase for 20 min at 37 °C, and precipitated in 400 mM ammonium acetate with 88% ethanol.

Whole-mount and fluorescence in situ hybridization (WISH and FISH) followed the established protocols.[74] Briefly, planarians were killed in 5% N-Acetyl-L-cysteine in PBS for 10 min, fixed in 4% formaldehyde with 1% NP-40 in PBS for 2 h, dehydrated in methanol, and stored at -20 °C for up to 1 month. Samples were rehydrated in PBST (0.3% Triton X-100 in PBS), bleached in bleaching solution (1.2% hydrogen peroxide, 5% formamide, and 0.5× SSC) under bright light for 2 h, permeabilized with 10 μg/mL proteinase K for 10 min, and post fixed with 4% formaldehyde for 10 min. The hybridization was performed with RNA probes overnight at 56 °C. The detection was through either alkaline phosphatase-catalyzed NBT/BCIP reaction (for WISH) or peroxidase-based tyramide signal amplification (for FISH).[74]

For immunostaining, planarians were killed, fixed, dehydrated, rehydrated, and bleached as described above. Subsequently, animals were blocked in 2% BSA in PBST for 2 h at room temperature and incubated with primary antibodies overnight at 4 °C. Animals were then washed 6 times with PBST, blocked again, and incubated with Peroxidase goat anti-mouse IgG+IgM antibody (1:1000) or Peroxidase goat anti-rabbit IgG (H+L) (1:1000) overnight at 4 °C. The signal was detected through peroxidase-based tyramide signal amplification.

Anti-phospho-Histone H3 (1:300) was used for H3P staining. Antibody 2G3-3D7 (1:200) was used for planarian muscle fiber staining. For single muscle cell FISH/immunostaining, animals were amputated to induce Erk activation and then dissociated at 3 hpa in CMF supplemented with a 1:10 dilution of Liberase TH into single cells[51] and processed as described above.

RNAi and drug treatment

dsRNA was prepared from *in vitro* transcription reactions using PCR-generated templates with flanking T7 promoters, followed by ethanol precipitation, and annealed after resuspension.[64] dsRNA was mixed with liver paste at a concentration of 100 ng/μl and fed to animals every 4 d for 10 times. The RNAi animals were starved for 7 d before experiments. In all RNAi experiments, dsRNA matching the *ccdB* and *camR*-containing insert of pJC53.2[64] was used as the negative control.

The irreversible Mek inhibitor, U0126, was first dissolved in DMSO to 10 mM and diluted in Instant Ocean to desired final concentrations. Animals were treated for 4 h before amputations, and Instant Ocean containing U0126 was refreshed daily throughout regeneration.

Experimental design

The single-cell sequencing data presented in the study was collected by pooling 30 animals into a single batch. All other experiments were repeated at least in three independent experiments using different samples to confirm results. This information is extensively described in figure legends. Animals were randomly selected from a large collection of clonal animals for all experiments. When evaluating phenotypes induced by drug or RNAi treatments, researchers were blind to sample allocation during experiments. No statistical method was used to predetermine sample size. No data was excluded from all analysis in this work.

Working model and alternative hypotheses

Our biological working model (Figure S5A) is as follows: First, a stimulus, such as a RTK ligand, is released from an upstream cell and binds to receptors at the proximal end of a muscle cell. We reasoned that a cell only needs to sense the signal in a small domain to activate the intracellular cascade. Indeed, Bastiaens and co-workers showed that a 0.8 μm sized bead with immobilized EGF was sufficient to stimulate a cell with EGF receptors on all parts of the cell rapidly activated within 10 s.[47] This suggests that the activation domain can be as small as 1 μm, and the time for two cells to communicate can be estimated by the time needed for ligands to diffuse across 1 μm. Assuming a slow extracellular diffusion coefficient, 0.1 $\mu m^2/s$,[19] this implies that the time needed for the signal to diffuse from one cell to the next should be on the order of ~10 s or longer.

Next, we suppose that one of two mechanisms rapidly spreads the activation of membrane-associated signaling molecules to the rest of the muscle cell. The Bastiaens group has presented evidence that there is double-negative feedback between the EGF receptor and a phosphotyrosine phosphatase, resulting in a trigger wave of EGF receptor activation spreading in the plane of the membrane.[47,48] In addition, Roose, Weiss, Chakraborty and co-workers have shown that active Ras can allosterically activate its upstream activator Sos, resulting in positive feedback and bistability in Ras activation in some cells.[49] This could lead to trigger waves of Ras activation. Either or both of these mechanisms could result in the rapid propagation of Ras activity down the full length of the muscle cell.

Then, the activation of membrane-bound Ras brings about the activation of the Raf-Mek-Erk cascade proteins in the cytoplasm. Studies over decades have shown that in animal cells with typical dimensions— cells a few pL in volume, with length scales of $\sim$10 μm— stimulation of RTKs or other upstream Erk regulators results in Erk activation within $\sim$5-10 min in various systems. This is most convincingly demonstrated in live cell imaging studies with fluorescent Erk reporters.[41,42] But even in the earliest studies of Erk activation, when 2D gels and western blots were the available tools, it was clear that Erk activation needs this amount of time. On the length scale of a typical cell ($\sim$10 μm), the transport time is negligible, a few seconds. The same should be true for planarian muscle cells, since they are only $\sim$5 μm in diameter. Thus this suggests a model where, within the time as dictated by the reaction kinetics of the Ras-Raf-Mek-Erk system, Erk should be activated everywhere within the muscle cell.

Finally, the release of intercellular activators from the distal end of this muscle cell activates the downstream cell. Two mechanisms have been proposed for how active Erk might then generate an intercellular signal.[44] One possibility is that it induces transcription, and the newly translated proteins are then transported throughout the cell, causing the release of RTK ligands.[75] This mechanism would be too slow to account for the rapid spread of Erk activation seen in the planarian. A second possibility, suggested by Matsuda and co-workers for the propagation of Erk activity in mammalian cells, is that active Erk molecules throughout the cytoplasm phosphorylate proteases, which in turn facilitate the secretion of activators into the extracellular space.[43] We suppose the second mechanism likely takes place in the planarian. This is followed by diffusion of this extracellular activator to the next muscle cell, on a time scale (as mentioned above) of $\sim$10 s.

In this model, we consider an intracellular cascade as the main route for transducing the signal from one end of a muscle cell to the other. This is because the extracellular diffusion of Erk activators is expected to be very slow, on the order of $\sim$0.1 $\mu m^2/s$.[18,19,37,45,46] Consider the alternative model that extracellularly diffusing activators can bind to more RTKs and induce the release of more activators, forming an extracellularly driven positive feedback,[35,76] the Luther relationship, $v \sim 2(D/\tau)^{1/2}$,[35,77] where v is the Erk wave speed, D is the extracellular diffusion coefficient, and τ is the doubling time of RTK activation, i.e., $\sim$5 min in this case as the release of activators requires Erk activation, implies that the propagation speed of Erk activity should be $\sim$ 130 μm/h. This is an order of magnitude slower than what we have observed in the planarian but roughly matches the speed observed in mouse skin epidermis.[18] This extracellular positive feedback model also predicts that the signal propagation speed should be independent of the geometry of propagating cells, which is inconsistent with our experimental observation that long muscles cells are the major cell type to propagate the signal. Finally, even assuming the fastest possible extracellular diffusion, which is $\sim$20 $\mu m^2/s$ for EGF/FGF molecules diffusing in water, the propagation speed for extracellular positive feedback should be on the order of $\sim$0.5 μm/s based on Luther's formula. In comparison, the intracellular propagation through the lateral RTK activation wave,[47,48] can have a speed of $\sim$2 μm/s, assuming that the diffusion coefficient of EGFR within the plasma membrane is $\sim$1 $\mu m^2/s$ and τ is $\sim$1 s for typical enzymatic reactions. Intracellular propagation still provides a faster route, and should be the dominant mechanism.

Mathematical modeling

To analytically estimate the cell size effect on trigger wave propagation, we consider the simplest case in which cells are densely packed in one dimension. In our model (Figure S5B), an upstream cell can produce activators that diffuse extracellularly to the target cell. Given the large length of the cell, we propose that only a fraction of cell body needs to sense the signal in order to activate the intracellular phosphorylation cascade in the entire cell body, which is a process much faster than the extracellular signal propagation.

Once activated, this cell then can release more activators into the extracellular space throughout its cell body to relay the signal to downstream cells. The partial differential equation that describes the normalized extracellular activator concentration $c(x,t)$ follows:

$$\frac{\partial c}{\partial t} = D\nabla^2 c + aH(c_{local} - C_{th})(1 - c). \quad \text{(Equation 1)}$$

Here D is the effective diffusion coefficient of the extracellular activator. The second term is a mean-field activation step function with activation threshold C_{th}. a is the effective release rate of the activator. H is the Heaviside step function. c_{local} is the local activator concentration near the upstream cell that the target cell senses. Term $(1 - c)$ sets the upper bound of activation. As the propagation of RTK activation and/or Ras activation across the length of a muscle cell should be much faster than the reaction kinetics of Erk activation, and thereby should not be the rate limiting step in propagating the signal, we chose not to model the intracellular transport process explicitly. Instead, we assume once the local activator concentration within a fraction of the cell exceeds C_{th}, the whole cell is activated and starts to produce the activator with an effective activator release rate to describe the intracellular reaction kinetics. The fact that the rate of production of activator is positively regulated by the activator concentration provides the system with the positive feedback required for trigger waves.

Given that activators are initially produced at a source (i.e., the wound), $c(x,t)$ should be a monotonic decreasing function of x, and therefore the fraction of cell body near the upstream cell should always sense the increase of activator concentration first. Assuming that a critical fraction of cell body (which has a length of d) needs to sense the activator before the cell gets activated (Figure S5B), the ansatz of the normalized signal concentration $c(x,t)$ is:

$$c(x,t) = c\left(r = \frac{x - vt}{l}\right), \quad \text{(Equation 2)}$$

where r is the distance from the wave front,[50,53] v is the wave speed, and $l = L/d$, which is the dimensionless cell length factor.

In the regime where $D \ll rv$, i.e., the displacement of signal front contributed by simple diffusion is negligible, the sensed activator concentration, $c^*(r)$, can be regarded as uniform across the entire cell body, and satisfies:

$$D\frac{\partial^2 c^*}{\partial r^2} + \frac{v}{l}\frac{\partial c^*}{\partial r} + aH(c^* - C_{th})(1 - c^*) = 0. \quad \text{(Equation 3)}$$

We treat Equation 3 as an ordinary differential equation.

For positions behind the wave front, $r < 0$, we have:

$$D\frac{\partial^2 c^*}{\partial r^2} + \frac{v}{l}\frac{\partial c^*}{\partial r} + a(1 - c^*) = 0. \quad \text{(Equation 4)}$$

For positions in front of the wave front, $r > 0$, we have:

$$D\frac{\partial^2 c^*}{\partial r^2} + \frac{v}{l}\frac{\partial c^*}{\partial r} = 0. \quad \text{(Equation 5)}$$

Assuming that the production of activators at the source remains constant during the whole process, we should have $r \to -\infty$, $c^* \to 1$. To satisfy this boundary condition, we solve Equation 4 and have:

$$c^*(r) = 1 - b_1 e^{\frac{r}{2D}\left(-\frac{v}{l} + \sqrt{\left(\frac{v}{l}\right)^2 + 4aD}\right)}. \quad \text{(Equation 6)}$$

Also, from the boundary condition $r \to \infty$, $c^* \to 0$, i.e., the normalized concentration of activator diminishes in regions where the wave front has not yet arrived, we solve Equation 5 and have:

$$c^*(r) = b_2 e^{-\frac{rv}{Dl}}. \quad \text{(Equation 7)}$$

With the assumption that c is continuous and has a continuous first derivative at the wave front, $r = 0$, comparing Equations 6 and 7 at $r = 0$ for $c(r = 0) = 0.5$, we have:

$$\frac{1}{2D}\left(-\frac{v}{l} + \sqrt{\left(\frac{v}{l}\right)^2 + 4aD}\right) = \frac{v}{Dl}. \quad \text{(Equation 8)}$$

Solving Equation 8 we have:

$$v = l\sqrt{\frac{aD}{2}}. \quad \text{(Equation 9)}$$

Altogether, the wave propagation speed $v \sim L\sqrt{aD}$. The important result here is that the speed scales with the cell length, as its dependence on D and a is consistent with previous studies.[50,53] This scaling relationship is also observed in our numerical simulations using the signaling relay model (Figures 6A and S6F–S6H).

Numerical simulation

To systematically investigate the effects of cell length, density, orientation, and diversity, we numerically simulate Erk activity propagation on a 2D plane where each cell occupies a specified space in a 2D lattice, using a recently developed diffusive signaling relay model.[53] Cells are activated when the concentration of activator within any lattice unit occupied by the cell exceeds a certain threshold (Figure S6A). The unit size is 10 μm by 10 μm and the smallest cells occupy one unit on the lattice.

In our simulation, for cells around the wound, the normalized concentration of the extracellular activator molecule $c(z,t)$ is set to be

$$\frac{\partial c}{\partial t} = D\nabla^2 c + \delta(z)a(1 - c), \quad \text{(Equation 10)}$$

where D is the effective diffusion coefficient of the extracellular activator, the Dirac function $\delta(z)$ accounts for space occupation of the cell, and $a(1 - c)$ is the source function accounting for the rate at which the signaling molecule is produced at the wound site. For

relay cells that are away from wounds, we assume $c(z,t)$ satisfies Equation 1. Here c_{local} in Equation 1 is the local concentration of activator within a lattice unit that the cell occupies. For receiving cells that only receive the signal without amplifying it:

$$\frac{\partial c}{\partial t} = D\nabla^2 c. \quad \text{(Equation 11)}$$

To simulate wave propagation, D was varied around 0.1 $\mu m^2/s$ based on previously inferred effective diffusion coefficients for extracellular Erk activators in a different biological context, regenerating fish scales.[19,37] This slow effective diffusion is justified by the narrow Erk wave width (< 1 mm) observed in our system, as fast diffusion would significantly broaden the wave front. Cell width was defaulted to be 10 μm and length was fixed at 10 μm for small cells but varied between 10–100 μm for long cells. Density of long cells was defined by the fraction of the 2D plane occupied by long cells. Orientation factor of long cells was defined by the fraction of long cells extending along the direction of wave propagation whereas other long cells are perpendicular to the wave direction.

Boundary conditions were set to be zero-flux for all simulations. Unless otherwise specified, signal release rate a was set to 12 s^{-1} and C_{th} was set to 0.1 in order to match the observed Erk wave speed. All simulations were performed on a 1 mm by 0.2 mm plane with 10 μm grid size. The simulation time step was 0.01 min. c was set to be 0 everywhere on the plane as the initial condition. Our simulation validated that this model can capture the essential dynamics of trigger waves (Figures S6B and S6C). Signal propagation speed was calculated through the mean displacement of the wave front, position at which average signal activity exceeds 0.1 (Figure S6C), per unit time.

QUANTIFICATION AND STATISTICAL ANALYSIS

Western blotting images were quantified using ImageJ Fiji software. Erk activation was measured by the ratio between pErk and total Erk and normalized to the 0 hpa activity in each group. The peak time of Erk activation was determined by fitting the activation vs. time with polynomials. Coefficient of determination (R^2) of polynomial fit was calculated using sklearn library with default parameters.

All statistical analyses were performed using Python (version 3.7.12) with sciPy library (version 1.9.3). Statistical methods used in each figure are reported in the figure legends. No method was used to determine whether the data met assumptions of the statistical approaches.

Supplemental figures

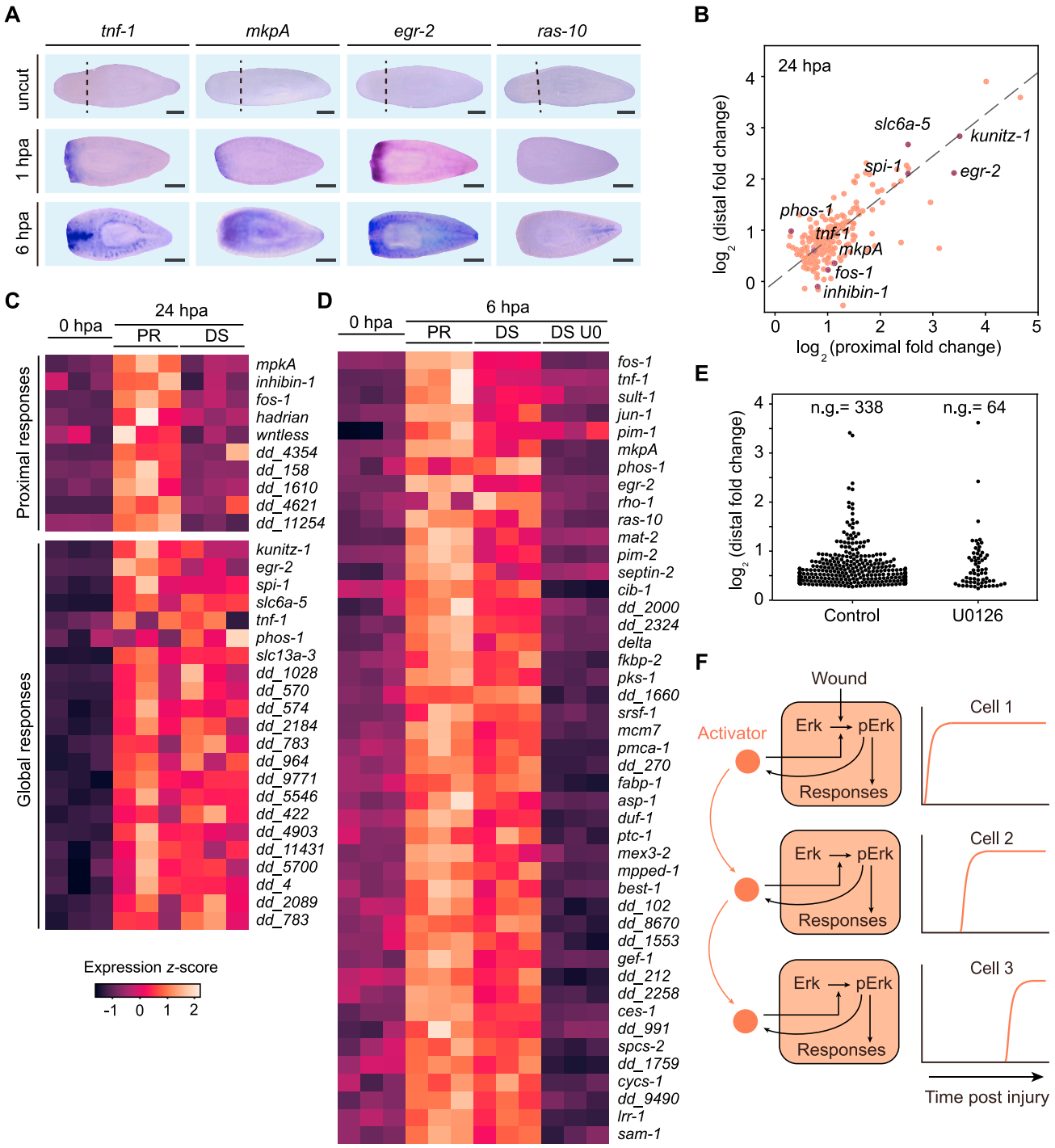

Figure S1. Systemic wound responses in planarian regeneration, related to Figure 1

(A) Whole-mount *in situ* hybridization (WISH) images showing activation of wound responses first in proximal and then in distal tissues. Induction of *ras-10* expression is specific in the tail only at 6 hpa. Dashed lines: amputation plane. Scale bars, 1 mm.

(legend continued on next page)

(B) Comparison of gene upregulation at 24 hpa in proximal and distal tissues. Fold changes were calculated from three biological replicates each containing five animals of ~5 mm in length. Each gene plotted has p value < 0.001 (two-sided Welch's t test) and $\log_2$(fold change) > 0.5 in either proximal or distal group. Note that the top upregulated genes are different from those observed at 6 hpa.
(C) Heatmap showing examples of upregulated wound response genes at 24 hpa.
(D) Heatmap showing examples of globally upregulated wound response genes at 6 hpa blocked by 25 μM U0126 treatment. PR, proximal; DS, distal.
(E) Fold changes of wound response genes at 6 hpa in distal tissues. U0126 treatment (25 μM) blocks the upregulation of ~80% of genes in distal tissues; n.g., number of genes.
(F) Schematic of Erk activity propagation. Activator (red) induces Erk phosphorylation. Activated Erk triggers transcriptional activation of wound responses and induces the release of more activators to extracellular space, which can induce positive feedback in the same cell, or diffuse to cells adjacent in space and trigger Erk activation therein.

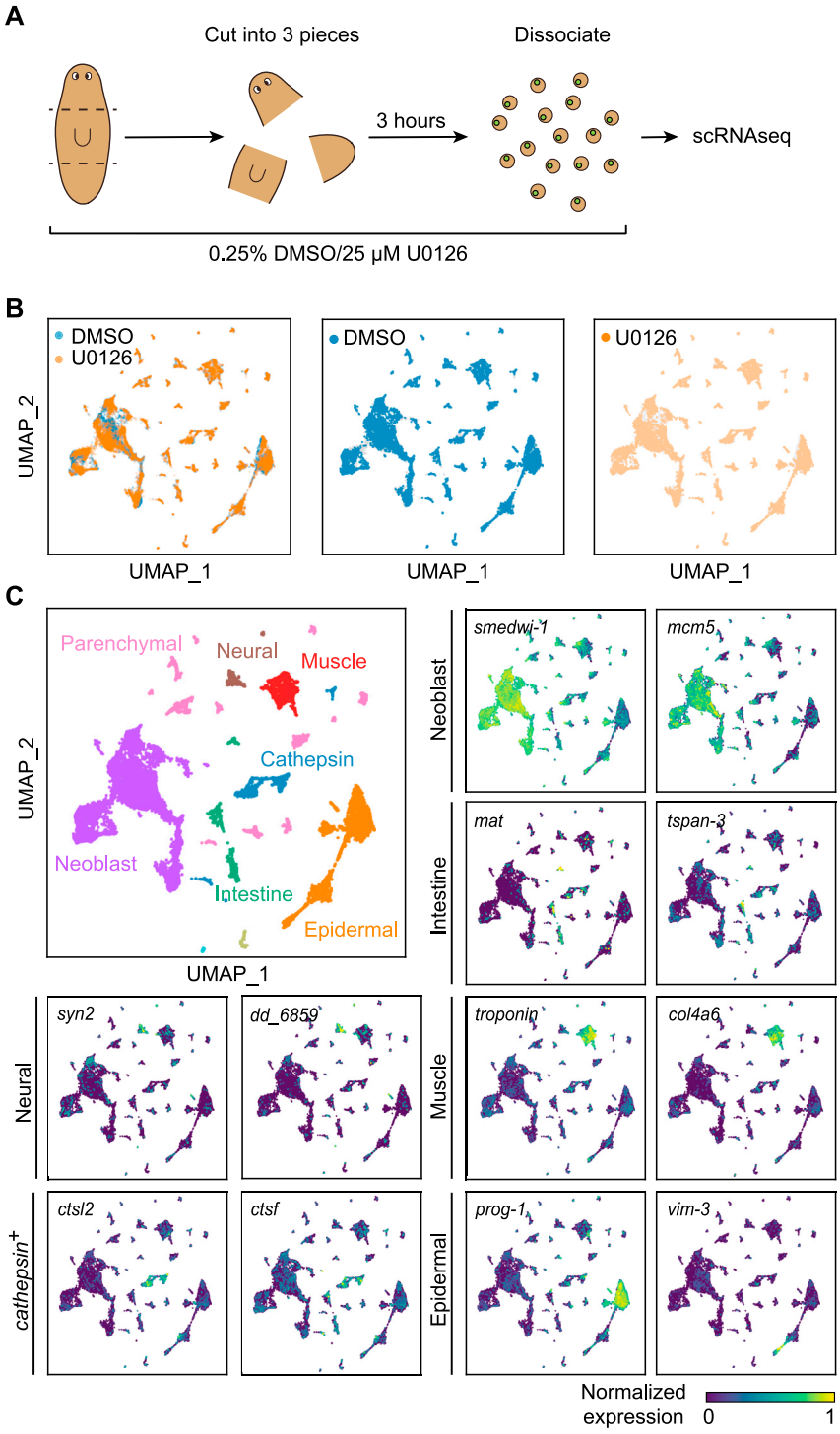

Figure S2. scRNA-seq captures cell-type-specific Erk-dependent wound responses, related to Figure 1

(A) Schematic showing the strategy to measure cell type-specific wound responses using scRNA-seq.

(B) UMAP projections of all cell clusters containing cells from both conditions: DMSO-treated (blue, 13,276 cells) and 25 μM U0125-treated (orange, 14,793 cells).

(C) Annotation of major cell types and example marker gene expression overlaid on the UMAP projection.

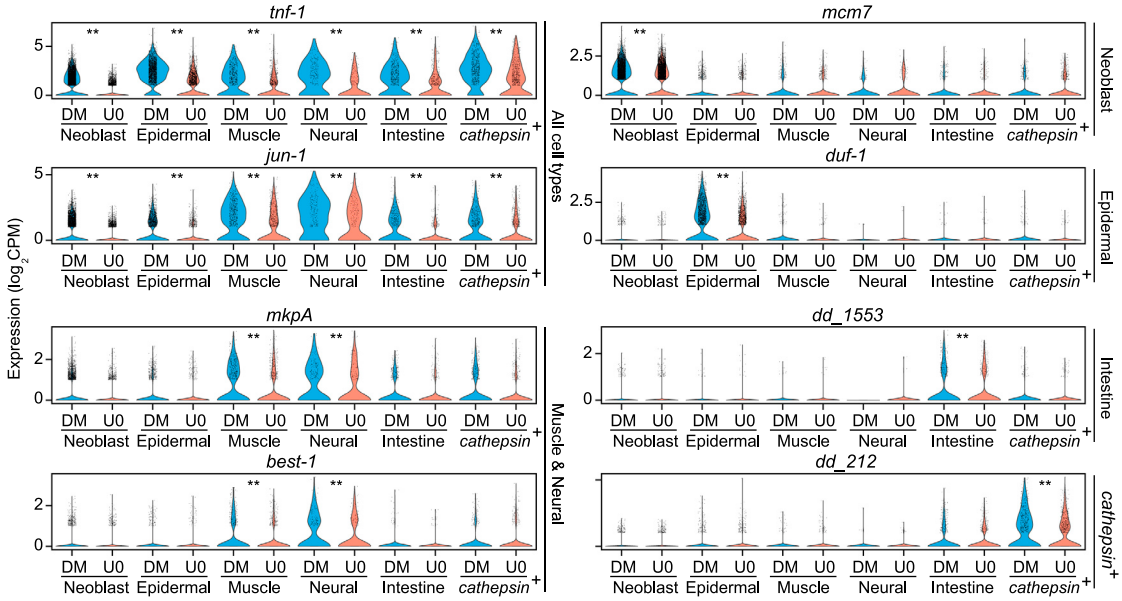

Figure S3. scRNA-seq identifies cell-type-specific Erk-dependent wound response genes, related to Figure 1

Violin plots showing the expression distribution of representative wound response genes in major cell types in animals. Blue/DM, DMSO-treated; orange/U0, 25 μM U0126-treated. Points: data of individual cells. **p < 0.01, two-sided Mann-Whitney-Wilcoxon test.

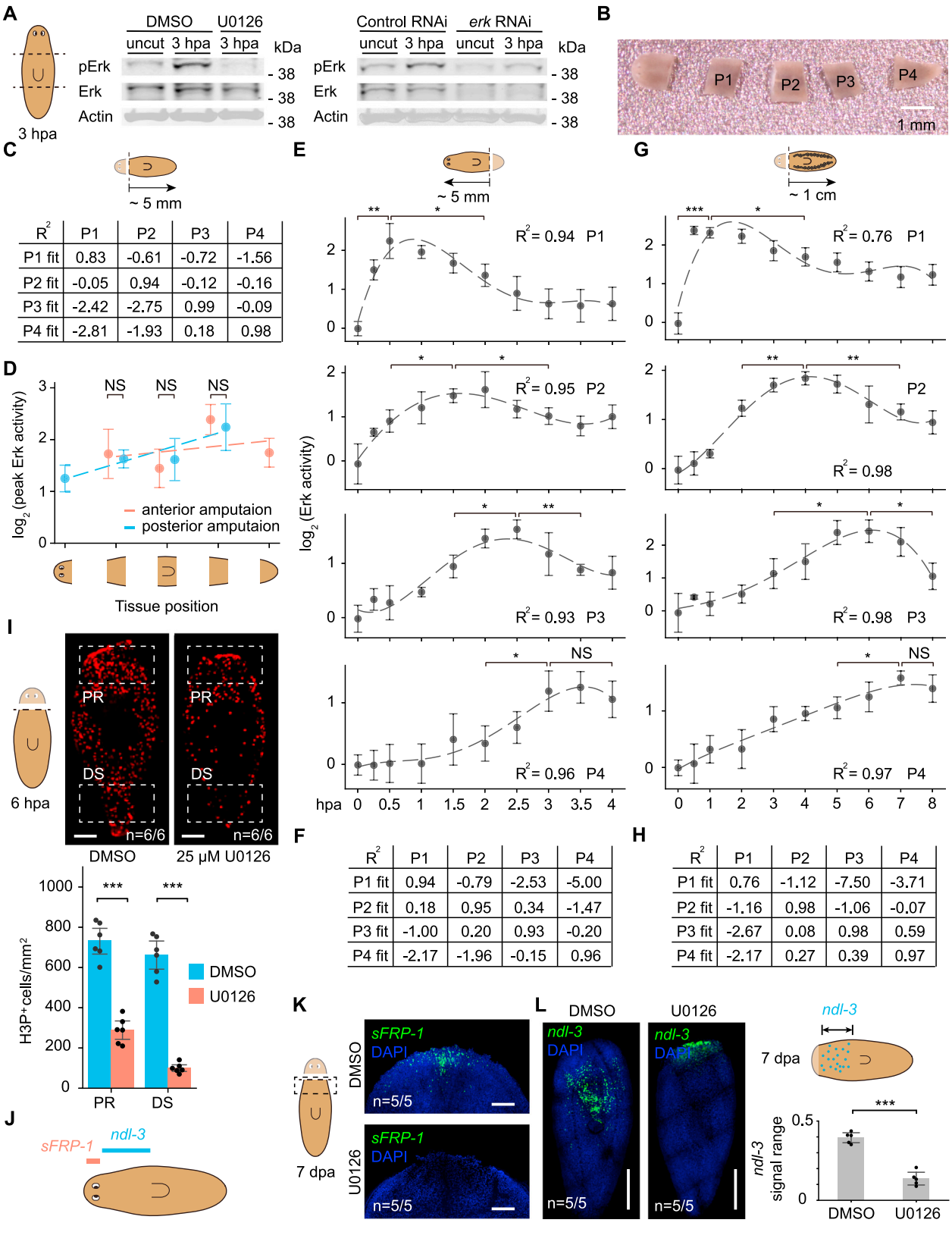

(legend on next page)

Figure S4. Erk activity propagation and its downstream effects, related to Figures 2 and 3

(A) Western blot images showing that 25 μM U0126 treatment eliminates pErk signal (left) and that *erk* RNAi decreases total Erk signal (right), validating the specificity of the antibodies.

(B) A representative image showing that a fixed worm is cut into pieces of ~1 mm in length for protein extraction.

(C) Coefficients of determination (R^2) for polynomial fit at each tissue position shown in Figure 2B. Each of P1–4 fits is determined on corresponding tissue pieces and then used to calculate R^2 for all other pieces. Each polynomial fit exhibits evident goodness specifically at its corresponding tissue position.

(D) Peak Erk activities in tissues with matched positions after anterior (orange) and posterior (blue) amputations. Peak activities at the same tissue position show no statistically significant difference after different amputations (NS, two-sided Welch's t test), suggesting that Erk signal does not dampen with distance traveled.

(E–H) Erk activity after posterior amputation on animals of ~5 mm in length (E) and anterior amputation on a sexual biotype with a longer body length of ~1 cm (G). Dashed lines: polynomial fit. Data were collected from three replicates using tissue fragments from ten animals. Coefficients of determination (R^2) of polynomial fit (P1–4 fit) are provided in (F) for (E) and (H) for (G).

(I) (Top) Anti-H3P labels mitotic cells at 6 hpa in animals treated with DMSO or 25 μM U0126. (Bottom) Number of $H3P^+$ cells counted in the proximal (PR) and distal (DS) regions (boxes in images). Animals are pooled from two independent experiments.

(J) Schematics showing the expression of position-control genes (*sFRP-1* and *ndl-3*) along anterior-posterior axis.

(K) The re-establishment of anterior *sFRP-1* expression is blocked by 8 μM U0126 treatment. Animals are fixed at 7 days post amputation (dpa) and pooled from two independent experiments.

(L) (Left) FISH images showing that *ndl-3* expression spreads posteriorly during regeneration, which is blocked by 8 μM U0126 treatment. Animals are fixed at 7 dpa and pooled from two independent experiments. (Right) Quantification of *ndl-3* expression range, normalized by the animal body length.

*$p < 0.05$; **$p < 0.01$; ***$p < 0.001$; NS, no significant difference; one-sided Welch's t test in (E) and (G); two-sided Welch's t test in (D), (I), and (L). Error bars: standard derivation (SD) in (D), (E), (G), and (L), 95% confidence interval in (I); n: number of samples consistent with the image out of the total number of samples analyzed. Scale bars: 1 mm in (B) and (L); 500 μm in (I); and 100 μm in (K).

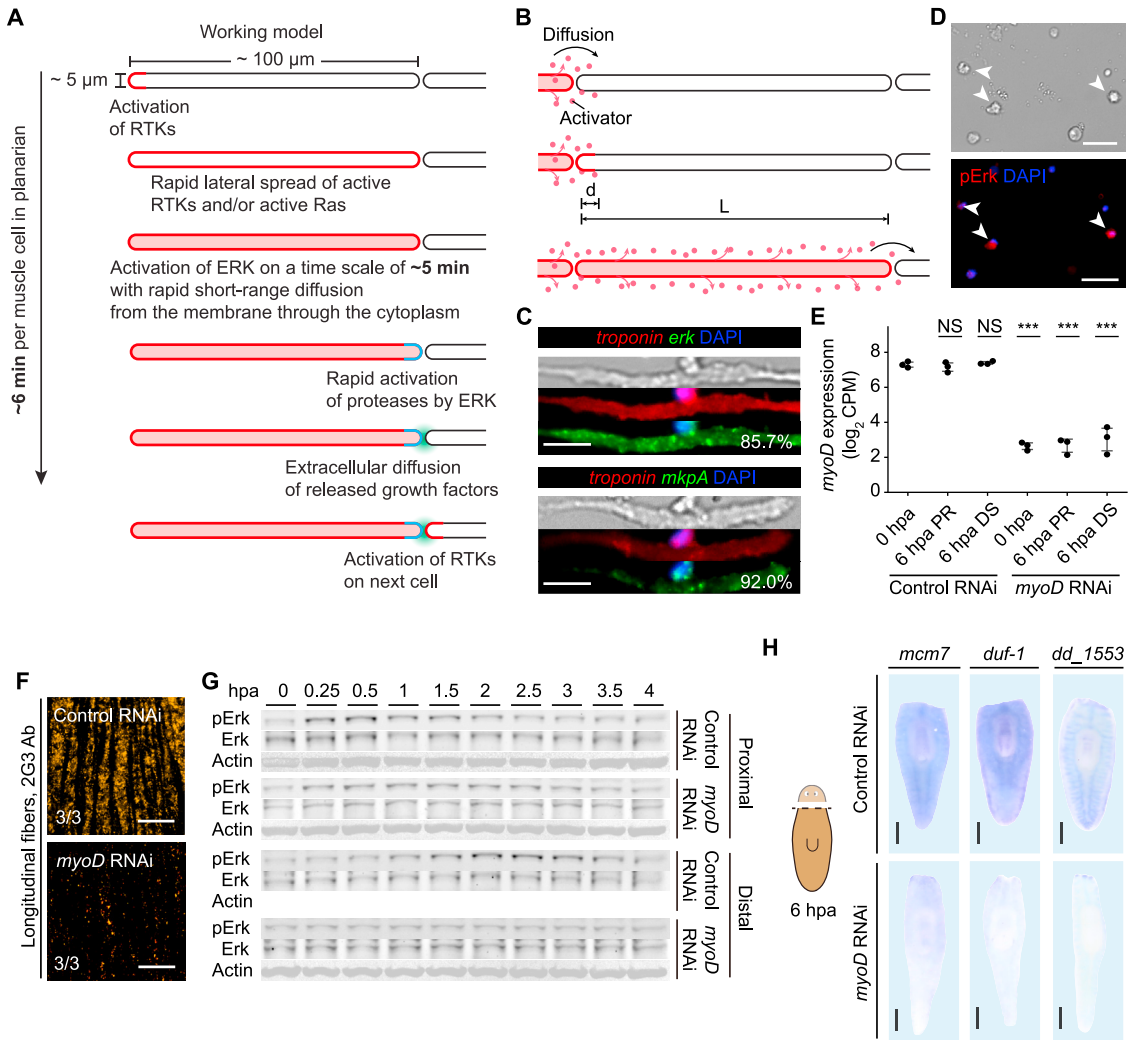

Figure S5. Muscles are essential for Erk activity propagation, related to Figures 5 and 6

(A) Schematic showing the biological processes involved in the signal relay between long cells (STAR Methods).

(B) Schematic showing the model used for analytical estimation (1D) and simulation (2D) (STAR Methods).

(C) Bright-field and double FISH images of isolated muscle cells (*troponin*$^{+}$, red) expressing *erk* (top, green) and *mkpA* (bottom, green), a conserved Erk-responsive dual-specificity phosphatases.[27,78] %, *erk*$^{+}$ and *mkp*A^{+} fractions of muscle cells.

(D) Bright-field and pErk immunostaining images of isolated cells to show cell types other than muscles can activate Erk pathway as well. Arrows: pErk^{+} cells.

(E) Normalized *myoD* expression measured by bulk RNA-seq, showing the efficiency of *myoD* knockdown. ***$p < 0.001$; NS, no significant difference, two-sided Welch's t test; error bars: standard derivation (SD).

(F) Immunofluorescence showing the loss of longitudinal muscle fibers in *myoD* RNAi animals.

(G) Representative images of western blotting against pErk, total Erk, and actin (loading control) showing Erk is not activated in tissues distal to wounds after *myoD* RNAi.

(H) WISH images showing activation of wound responses in control RNAi animals throughout the body (top) but restricted to injury site after *myoD* RNAi (bottom) at 6 hpa.

Scale bars: 20 μm in (C) and (D); 10 μm in (F); and 1 mm in (H).

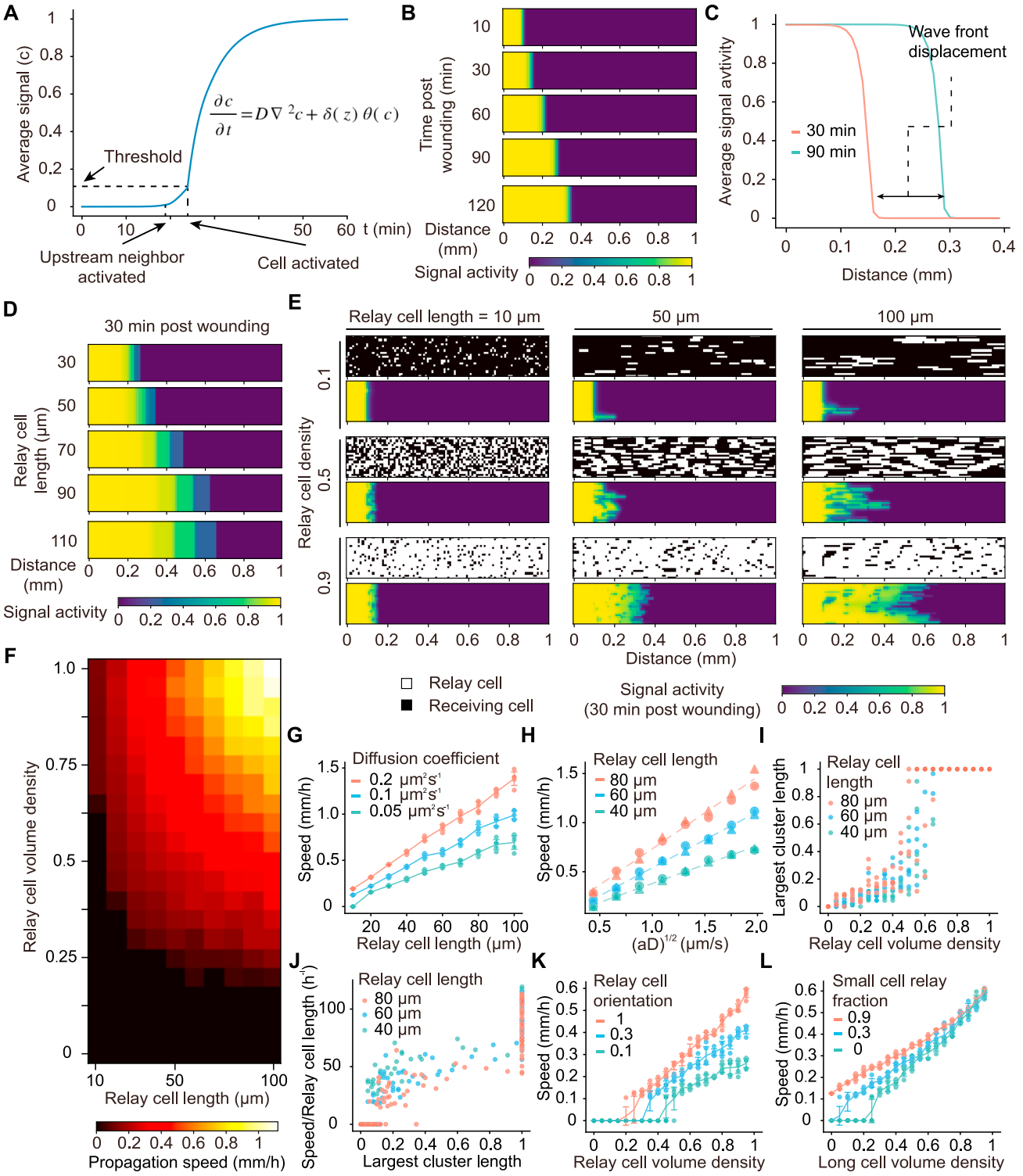

Figure S6. A diffusive signaling relay model to simulate biochemical activity propagation in heterogeneous tissues, related to Figure 6

(A) Single-cell signaling activation dynamics during wave propagation. The times of activation are defined by when activator concentration in the lattice unit close to the upstream neighbor exceeds the threshold, C_{th}.

(B) Simulated wave propagation at a speed of ~150 μm/h.

(C) Mean signal activity vs. position. Wave fronts are defined at the position where mean signal activity exceeds 0.1. Wave speed is calculated by the displacement of wave fronts per unit time.

(legend continued on next page)

(D) Erk activity propagates faster through longer cells. These simulations contain densely packed cells with uniform lengths.
(E) Spatial distributions of signal relay cells (white, top) and signal activity (bottom) in heterogeneous tissues with varying long cell lengths and volume densities. Note that cells that do not relay signal also can be activated.
(F) Heatmap showing the speed of signal propagation increases with relay cell length and volume density.
(G) The trend that signal propagation speed increases with relay cell length is robust to varying ligand diffusion coefficient. Long cell volume density is fixed at 0.9.
(H) Signal propagation speed scales with $(aD)^{1/2}$ (dashed lines), regardless of relay cell length. Circles: a = 12 s^{-1}, D varies from 0.016 to 0.4 $\mu m^2/s$; triangles, D = 0.1 $\mu m^2/s$, a varies from 1.92 to 48 s^{-1}. Long cell volume density is fixed at 0.9.
(I) Length of the largest long cell cluster along the direction of wave propagation, normalized by the simulation plane length, vs. relay cell volume density.
(J) Replotting the data in (I) to show that the signal propagation speed increases with the length of the largest long cell cluster.
(K) Signal propagation speed increases with relay cell density in simulations varying long cell orientation factors.
(L) Signal propagation speed increases with long cell volume density in simulations varying fractions of small cells that can relay the signal.
Error bars: standard derivation (SD) calculated from five simulations with long cells randomly positioned in 2D space. In all simulations shown in (E)–(K), small cells only can receive but cannot relay signal. Orientation factor is fixed at 1 except for (K). In (K)–(L), long cells are 50 μm in length.